Hydroxyapatite reinforced inorganic-organic hybrid nanocomposite as high-performance adsorbents for bilirubin removal *in vitro* and in pig models

Yamin Chai [a], Zhuang Liu [a], Yunzheng Du [a], Lichun Wang [a], Jinyan Lu [a], Qian Zhang [a], Wenyan Han [a], Tingting Wang [a], Yameng Yu [a], Lisha Sun [b], Lailiang Ou [a,*]

[a] *Key Laboratory of Bioactive Materials, Ministry of Education, College of Life Sciences, Nankai University, Tianjin, 300071, China*
[b] *General Hospital, Tianjin Medical University, Tianjin, 300052, China*

ARTICLE INFO

ABSTRACT

Highly efficient removal of bilirubin from whole blood directly by hemoperfusion for liver failure therapy remains a challenge in the clinical field due to the low adsorption capacity, poor mechanical strength and low biocompatibility of adsorbents. In this work, a new class of nanocomposite adsorbents was constructed through an inorganic-organic co-crosslinked nanocomposite network between vinyltriethoxysilane (VTES)-functionalized hydroxyapatite nanoparticles (V-Hap) and non-ionic styrene-divinylbenzene (PS-DVB) resins (PS-DVB/V-Hap) using suspension polymerization. Notably, our adsorbent demonstrated substantially improved mechanical performance compared to the pure polymer, with the hardness and modulus increasing by nearly 3 and 2.5 times, respectively. Moreover, due to the development of a mesoporous structure, the prepared PS-DVB/V-Hap3 exhibited an ideal adsorption capacity of 40.27 mg g^{-1}. More importantly, the obtained adsorbent beads showed outstanding blood compatibility and biocompatibility. Furthermore, *in vivo* extracorporeal hemoperfusion verified the efficacy and biosafety of the adsorbent for directly removing bilirubin from whole blood in pig models, and this material could potentially prevent liver damage and improve clinical outcomes. Taken together, the results suggest that PS-DVB/V-Hap3 beads can be used in commercial adsorption columns to threat hyperbilirubinemia patients through hemoperfusion, thus replacing the existing techniques where plasma separation is initially required.

1. Introduction

Bilirubin, an indicator of liver function levels, is primarily derived from the metabolites of hemoglobin released by decrepit red blood cells. Under normal circumstances, it is transported to the liver as a complex with albumin to form water-soluble macromolecular complexes with a diameter of approximately 7 nm (indirect bilirubin, IBIL) and excreted from hepatocytes into bile mainly in a glucuronide-conjugated state (direct bilirubin, DBIL) [1–4]. The normal total bilirubin (TBIL) level in serum is 1–10 g L^{-1} [5]. However, disorders in its successive metabolism and/or excretion may cause excess accumulation of unconjugated bilirubin in the blood of patients who suffer from liver diseases such as acute hepatic failure, hepatitis, and neonatal pathologic jaundice (hyperbilirubinemia) [4,6]. The extra bilirubin could cause mental retardation, hepatic coma, deafness, hearing loss, epilepsy, permanent brain damage, or even result in death in severe cases [7,8].

For most of the past few decades, plasma perfusion has been demonstrated to be an effective strategy to lower bilirubin levels, and the treatment has been successfully used in clinics to induce remission of liver disease and to gain time for patients waiting for orthotopic liver transplantation (OLF) [4,9–11]. Currently, a series of bilirubin adsorbents have been developed, as the adsorbent system is a critical component of plasma perfusion [12]. For example, conventional adsorbents such as activated carbon (AC) and anion exchange resins have been exploited as adsorbents in hemoperfusion columns for the treatment of hyperbilirubinemia [12–14]. However, such adsorbents have limited hemocompatibility. AC may induce platelet activation and a decrease in platelet and white blood cell counts once it contacts blood,

and this may place the patients at high risk of bleeding or other severe side effects [15,16]. Anion exchange resins such as Plasorba BR-350 (Asahi Medical, Osaka, Japan) [17], which can efficiently remove bilirubin based on electrostatic interactions, will also clear heparin, citric acid, and other anionic anticoagulants, with the possibility of disturbing the homeostasis of the plasma pH [18]. As a result, both of the above adsorbents must be operated on the basis of a plasma separation system rather than from whole blood, which unfortunately limits their clinical applications because of the complicated nature of the procedures [19, 20]. Additionally, novel chemically designed materials such as synthetic bilirubin imprinted polymers (MIPs) [20,21], silica [22], aerogel beads [23], metal-organic frameworks (MOFs) [24], and functionalized polymer microspheres [25] have also been investigated; these have shown promising results. These adsorbents, however, often have unsatisfactory adsorption performance, weak mechanical strength, and poor stability resulting in reduced therapeutic efficacy. Furthermore, most of these adsorbents come in the form of powders, which also limits their practical adsorption application. Therefore, bilirubin adsorbents with excellent adsorption performance, hemocompatibility, and high mechanical strength for effective removal of bilirubin directly from whole blood are still in strong demand.

Recently, copolymers of non-ionic styrene-divinylbenzene (PS-DVB) resins have been developed with suitable size, well-developed pore structure, high specific surface area, low toxicity, and good blood compatibility, making them appropriate as adsorbents for removing toxins from plasma [13,26,27]. Nevertheless, PS-DVB has drawbacks, such as limited adsorption capacity and weak mechanical properties, which are major limitations to its further application, especially for whole blood hemoperfusion. To endow polymers with improved mechanical properties and other valuable characteristics, introduction of nanomaterial fillers has been considered as an effective strategy [28–30]. For example, Ye and colleagues reported the generation of phenolic-resin-derived activated carbon-based CNTs composite spheres (CNTs/P-ACSs) with highly effective removal of VB$_{12}$. This material possesses enhanced mesoporous volume and mechanical strength [31]. In our previous work, a polystyrene/nano-CaCO$_3$ (PS/nCaCO$_3$) composite with enhanced mechanical strength was developed by incorporating nCaCO$_3$ into PS resin. The results showed that PS/nCaCO$_3$ exhibited increased mesoporous volume and surface area, yielding enhanced IL-6 adsorption capacity [32]. To date, hydroxyapatite (Ca$_{10}$(PO$_4$)$_6$(OH)$_2$, Hap), a type of hydroxylated calcium phosphate-based biomaterial, has been used to reinforce mechanical strengths of polymeric matrices due to its mechanical properties, biocompatibility, and noninflammatory and nontoxic properties [33, 34]. These factors, together with the high specific surface area and promising chemical and physical properties of the material [35,36], suggest that Hap may benefit both the adsorption capacities and mechanical properties of PS-DVB in the removal of bilirubin. Unfortunately, it is well-known that bare nano-Hap is liable to form aggregates in the polymer matrix as a result of interparticle van der Waals forces and hydrogen bonding between surface hydroxyl groups, which may lead to inhomogeneous dispersion and decrease the mechanical properties and biocompatibility of the resultant nanocomposites. This may further limit practical applications of Hap as adsorbents for use in hemoperfusion: nanoparticles would inevitably leak into the patient's blood, causing thrombosis and thus blocking blood vessels. In addition, it is difficult to separate and recycle the particles from blood, and this would cause secondary pollution. To overcome such drawbacks, increasing the hydrophobicity of Hap by modification with vinyl to form covalent bonds with organic polymers should be an effective solution and thus improve the biocompatibility of Hap-polymer composites.

In this study, vinyltriethoxysilane (VTES) was used to modify the surfaces of the particles due to its low toxicity and high hydrophobicity [37]. As shown in Fig. 1, the reactive VTES-conjugated Hap (V-Hap) was designed (1) to enhance the hydrophobicity, stability, and dispersion of the nanofiller and prevent the precipitation of the filler; (2) to covalently
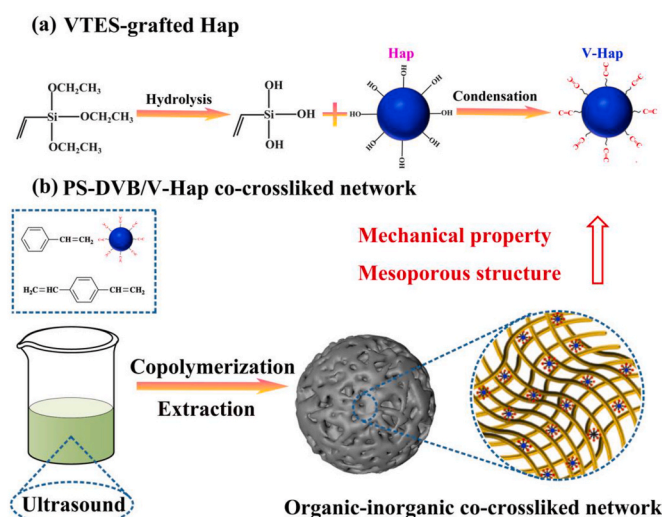
Fig. 1. Schematic illustration of synthesis routes of (a) VTES-grafted Hap, and (b) PS-DVB/V-Hap nanocomposite. The Hap with reactive VTES chains was designed to covalently interact with PS-DVB and form an organic-inorganic co-crosslinked network within the nanocomposite; this was expected to improve the mechanical strength and promote the development of a mesoporous structure.

crosslink with a polystyrene-divinylbenzene matrix for the immobilization of modified Hap to improve the interfacial bonding between the Hap and the polymer matrix as well as increase the adsorptive capacity and enhance the mechanical strength of the novel PS-DVB/V-Hap adsorbent for bilirubin removal in hemoperfusion. To the best of our knowledge, the pore structure is the primary influencing factor that affects the adsorption performance [38]. As expected, by simple changing the content of V-Hap, we obtained appropriate strength and a highly developed mesopore structures of the material that can accommodate and effectively remove more bilirubin molecules, since this will provide more space for the free bilirubin and the indirect bilirubin to access the resin beads. Considering the albumin-binding properties of bilirubin and the fact that various salt ions in human plasma lead to high ionic strength, this may inhibit the removal of bilirubin during the hemoperfusion process [39]. A conformational change takes place in the bilirubin molecule when the temperature changes, resulting in a certain effect on the adsorption efficiency [40]. Thus, the effects of albumin concentration, solution ionic strength, and temperature on the adsorption characteristics *in vitro* were studied in order to optimize the sorption performance and elucidate the mechanism involved in the process. Furthermore, a pseudo-first-order kinetic model and a pseudo-second-order kinetic model were applied to study the dynamic adsorption performance, while the Langmuir and Freundlich models were applied to describe the adsorption process. Biocompatibility tests and *in vivo* hemoperfusion for bilirubin removal from whole blood in pig models were carried out and are discussed in detail. In brief, a series of *in vitro* and *in vivo* studies demonstrated that our nanocomposite has high mechanical strength and effective adsorption capability, outstanding blood compatibility, and low cytotoxicity. In addition, there were no obvious changes in physicochemical properties before and after hemoperfusion. These features make the spheres highly promising for clinical whole blood perfusion and artificial liver construction.

2. Materials and methods

2.1. Materials

All reagents and anhydrous solvents of analytical purity were commercially available and were used as received unless otherwise

indicated. Nano-Hap and VTES were purchased from Aladdin (Shanghai, China). Bovine serum albumin (BSA) was obtained from Tianjin Keke Biotechnology Co., Ltd (Tianjin, China). Bilirubin was obtained from Sigma-Aldrich (Shanghai, China). Poly (vinyl alcohol) (PVA) was received from Macklin (Shanghai, China).

2.2. Preparation of V-Hap

V-Hap with reactive brushes was prepared by grafting vinyltrimethoxysilane to the surface of Hap by a hydrolysis-condensation process [30] (Fig. 1a). Briefly, 1 mL of VTES was added to 10 mL of aqueous ethanol solution and mixed under magnetic stirring for 60 min. Then, 1 g Hap was thoroughly dried at 120 °C for 48 h before being added to the solution under continuous stirring and left to react at 70 °C for 8 h under nitrogen. Finally, the mixture was adjusted to pH 10.0 by sodium hydroxide solution (0.1 M). The VTES-grafted Hap (V-Hap) was then separated by centrifugation at 5000 rpm, thoroughly washed with deionized water and alcohol, and dried at 40 °C under a vacuum for 24 h to prepare PS-DVB/V-Hap.

2.3. Synthesis of PS-DVB/V-Hap composites

A certain amount of V-Hap was added to the oil phase that contained styrene (monomer), divinylbenzene (cross-linker), toluene and liquid wax at a 2:1 ratio (porogen), and benzoperoxide (initiator) in a ratio range of 3:5:92:250:1. The mixture was dispersed by ultrasonication for 30 min to form a homogenous oil phase (Fig. 1b). After that, the obtained mixture was quickly added into a solution of 500 mL 2 wt% PVA aqueous solution with stirring at 120 rpm for 30 min at 45 °C to obtain uniform small droplets. Then, the temperature was slowly raised to 80 °C with a ramp rate of 0.4 °C min^{-1} and kept at 80 °C for 3 h, then increased to 95 °C for 5 h with a ramp rate of 2 °C min^{-1}. The obtained solid was washed with hot water several times under continuous stirring to remove the dissolved components. Afterward, the pore-foaming agent was extracted using a Soxhlet extractor with an excessive amount of petroleum ether at 100 °C for 48 h. Then, the inorganic-organic co-crosslinked polystyrene-divinylbenzene beads were washed with ethanol and water three times. Finally, the obtained adsorbent as PS-DVB/V-Hap3 was dispersed in ethanol or water for further studies. For comparison purpose, PS-DVB/V-Hap nanocomposites with different concentrations of V-Hap (0, 1, 2, 4 and 5 wt%) were also prepared using the same method and labelled as PS-DVB, PS-DVB/V-Hap1, PS-DVB/V-Hap2, PS-DVB/V-Hap4 and PS-DVB/V-Hap5, respectively.

2.4. Characterization of V-Hap and PS-DVB/V-Hap

Fourier transform infrared spectroscopy (FTIR, Nicolet iS50, USA), a thermogravimetric analyzer (TGA, Netzsch, Germany), an X-ray diffractometer (XRD, Rigaku, Japan), and energy-dispersive X-ray spectroscopy (EDS) analysis (EDXA Octane Elect Super, USA) were employed for chemical characterization of the non-grafted Hap and grafted V-Hap. For the PS-DVB/V-Hap spheres, FTIR, XRD, TGA, EDS, Field Emission Scanning Electron Microscope (FESEM, Apreo S LoVac, USA), and High-resolution Transmission Electron Microscope (HRTEM, FEI Tecnai F20 EM) were employed for characterization. Nano-indentation experiments were carried out by an Agilent G200 Nano Indenter to study the macroscopic mechanical properties of adsorbents. The pore porosity was determined by the analysis of three SEM surface images containing at least three hundred pores using ImageJ software (Rawak Software, Inc., Germany) and was calculated according to the following equation [41]:

Porosity factor (%) = S$_p$/S$_m$ *100

where S$_p$ and S$_m$ are the total area of pores and the area of support surface in the same SEM image, respectively. The surface area was

calculated by BET (Brunauer-Emmett-Teller, BEL sorp miniX, Japan) while the pore size distribution was obtained using desorption branch of isotherms based on Barrett-Joyner-Halenda (BJH) method at 77 K. The total pore volume (T$_p$) was conducted on at P/P$_0$ = 0.99 according to Gurwitsch's rule [42]. Inductively coupled plasma optical emission spectroscopy (ICP-OES, SpectroBlue) was used to measure the V-Hap content in PS-DVB/V-Hap. Before measurements, the adsorbents were adjusted to 45 °C for 24 h, and sufficient water was removed.

2.5. Adsorption experiments in vitro

2.5.1. Adsorption experiments in simulate serum

The volume ratio of adsorbents to solution was 1:20. The effect of a series of PS-DVB/V-Hap adsorbents with different contents of V-Hap (5, 4, 3, 2, 1 and 0 wt%) on the adsorption of bilirubin was investigated. The adsorption kinetics and isotherms were utilized to analyze the adsorption mechanism. Then, the effects of temperature and ionic strength on the adsorption of bilirubin were explored. Since bilirubin is an albumin-bound toxin and the presence of albumin significantly inhibits bilirubin uptake during the hemoperfusion process, the bilirubin adsorption capacity in a bovine serum albumin-rich solution was also evaluated. The experimental details are shown in the Supporting Information.

2.5.2. Research on bilirubin adsorption in human plasma

The adsorption properties of adsorbents in the plasma of hyper-bilirubinemia (supplied by Second Affiliated Hospital of Tianjin University of TCM) were tested. The volume ratio of the adsorbents to the plasma was 1:6; Then, the plasma was shaken at a speed of 160 rpm for 2 h at 37 °C. After adsorption, the solution was left to stand for 5 min, and the supernatant was obtained and sent to the hospital to measure the concentrations of TBIL, DBIL and IBIL.

2.6. Biosafety assessment of PS-DVB/V-Hap

2.6.1. Blood compatibility testing

Before measurements, the adsorbents were immersed in normal solution (NS, 0.9% NaCl) overnight. To test the hemolysis of adsorbents, 3 mL of rabbit blood was taken from the ear vein, and the blood was diluted according to anticoagulation: normal saline = 4:5 to obtain a red blood cell suspension. A negative control group, a positive control group, and an experimental group received 5 mL NS, 5 mL distilled water, and 2 g adsorbents, respectively. Each group had 100 μL red blood cell suspension added and kept at 37 °C for 1 h. The solutions were then centrifuged at 2500 rpm, and the supernatant was used to measure the absorbance at 545 nm. Finally, the hemolysis ratio was calculated using the formula provided in previous studies [32]. To test the blood routine, 2 mL of blood from a rabbit heart was added to the EDTA·K$_2$ anticoagulated blood collection tubes, and then 0.2 g adsorbent was added, and the tube was gently shaken. The whole blood was used as a control sample. All the blood collection tubes were incubated in a 37 °C constant temperature water bath for 1 h. The blood was carefully aspirated, and routine blood parameters were measured with a fully automatic blood cell counter. The activated partial thromboplastin time (APTT) and thrombin time (TT) were measured to investigate the anti-coagulant properties of the PS-DVB/V-Hap, and the process was as follows: 4 mL blood from a rabbit heart was added to the sodium citrate anticoagulated blood collection tubes, then centrifuged at 4000 rpm for 15 min to obtain platelet-poor plasma (PPP). Then 2 mL of PPP was added to 0.2 g of adsorbents and gently shaken at 37 °C for 1 h. Pure PPP without sample was the control treatment. All measurements were carried out six times. The tests were performed by a semiautomatic blood coagulation analyzer CA-50 (Sysmex Corporation, Kobe, Japan). Furthermore, to assess blood biochemical properties, 1 mL of adsorbent was incubated with 6 mL of plasma at 37 °C for 2 h. A 1 mL volume of NS was used as a control and was also incubated for comparison. The levels of major serum proteins and ion concentrations in the supernatants were

measured by an URIT-8260.

2.6.2. Cytotoxicity testing

The NIH3T3 cells were grown in Dulbecco's Modified Eagle medium (DMEM) supplemented with 10% fetal bovine serum (FBS) and 1% antibiotics (penicillin-streptomycin) at 37 °C in a humidified incubator containing 5% CO_2. A standard CCK-8 assay was used to assess the cytotoxicity of PS-DVB and PS-DVB/V-Hap3. Before the measurement, the adsorbents (2 g) were pre-immersed in DEMA (10 mL) and incubated at 37 °C for 24 h, then filtered and sterilized with a 0.22 μm microporous membrane to obtain the supernatants. Cells at required density (1×10^3 cells well^{-1}) were seeded in 96 well plates for 24 h. After washing with PBS, 100 μL of supernatants was added into the culture medium and incubated at 37 °C for 72 h under above conditions. The negative control group was incubated with 100 μL culture medium DMEM instead of adsorbents. The positive control group comprised 100 μL cell culture medium containing 5% DMSO. Soon after treatment, the liquid was discarded; 10 μL of CCK-8 was added to the culture medium, and the resulting solution was incubated at 37 °C for 2 h. The cell viability was determined by measuring the optical density at 450 nm on a multimode plate reader (PerkinElmer EnSpire) [43] and calculated as the relative value-added rate (RGR) based on the following formula:

RGR (%) = A/A$_0$*100

Where: A and A_0 are the OD values of experimental group and negative control group, respectively.

The evaluation criterion was as follows: the cytotoxicity corresponding to the positive control group was required to be at least grade 3.

2.7. In vivo therapeutic efficacy evaluation

All animal experiments were reviewed and approved by the Institutional Animal Care and Use Committee (IACUC) of First Central Hospital of Tianjin and Nankai University. Bama miniature pigs (1 year old), weight 35 ± 10 kg, no limits for males and females, were kept under pathogen-free conditions for seven days. Experimental procedures were conducted under general anesthesia induced by intramuscular injection of 5% pentobarbital (10 mg kg^{-1}). Heparin administration is also standard medical practice in humans receiving extracorporeal hemoperfusion. To induce hyperbilirubinemia, pigs were given a single operation that involved locating the bile duct along the hepatoduodenal ligament, a double ligation of the bile duct above the duodenum, and abdomen closing. Seven days after hyperbilirubinemia was induced and the concentration of TBIL reached approximately 100 μmoL L^{-1}, the pigs with successful modeling were treated with a PS-DVB/V-Hap hemoperfusion cartridge at a flow rate of 60 mL min^{-1} for 2 h. In the treatment with the hyperbilirubinemia hemoperfusion cartridge, 10 mL venous blood was taken at time points of 10, 30, 45, 60, 90 and 120 min, and 10 mL arterial blood was taken after the operation to measure the level of bilirubin and analyze the indices of liver and kidney function as well as routine blood parameters.

2.8. Statistical analysis

All results are presented as mean ± SD, as noted in the text. After meeting assumptions for normality (tested with the Shapiro-Wilk test), the statistical significance of differences between datasets was evaluated using one-way ANOVA with post hoc Tukey's multiple comparisons test in GraphPad Prism (GraphPad Software Inc.) and group comparisons using paired sample t tests. A significant p-value indicates a probability less than 0.05 (*$p < 0.05$), 0.01 ($0.05 < **p < 0.01$), 0.001 ($0.01 < ***p < 0.001$), and 0.0001 ($0.001 < ****p < 0.0001$).

3. Results and discussion

3.1. Characterization of Hap and V-Hap

Detailed of the synthesis and characterization of V-Hap are shown in Fig. 2. The non-grafted Hap and grafted V-Hap were characterized to verify the coupling of the VTES chain to the Hap surface using FTIR measurements (Fig. 2a), and the attributions of all absorption peaks are summarized in Table S1. The Hap showed strong characteristic P–O stretching absorption peaks at 1096, 1035, and 962 cm^{-1}, and bending absorption peaks at 608 and 560 cm^{-1} [44,45]. Notably, there was a sharp absorption peak at 3570 cm^{-1} that was assigned to the O–H stretching vibration, and the peak at 3430 cm^{-1} was due to the presence of adsorbed water [46]. For VTES, the absorption peaks at about 3068 and 2944 cm^{-1} were attributed to the asymmetrical stretching vibration (ν_{as}) of $=$ C–H group and stretching vibration (ν_s) of –OCH$_2$CH$_3$ group. The double peak at 1610 and 1413 cm^{-1} corresponded to C$=$C stretching vibration in the vinyl group [47]. The V-Hap possessed a similar FTIR spectrum to Hap. The characteristic peaks of V-Hap were nearly unchanged in comparison to pure Hap [48]. After the introduction of VTES, the –OH peak at 3570 cm^{-1} nearly disappeared, while the characteristic peaks of VTES (1620 and 1420 cm^{-1} for C$=$C group, 3065 cm^{-1} for $=$ C–H group, and 2950 cm^{-1} for –OCH$_2$CH$_3$ group) appeared in V-Hap, confirming the successful synthesis of V-Hap. More importantly, new characteristic absorption peaks appeared at 1100 cm^{-1} and 780 cm^{-1}, indicated Si–O–Si and P–O–Si formation in modified Hap attributed to two reactions between Si–OH and hydroxyl groups and between Si–OH and HPO$_4^{2-}$ groups, respectively [30,37,49].

The crystalline structures of the non-grafted Hap and grafted V-Hap were further identified using XRD. The XRD pattern of the Hap and V-Hap remained nearly the same with characteristic diffraction of (0 0 2), (2 1 1), (3 0 0), (2 0 2), (3 1 0), (2 2 2), and (2 1 3) without the presence of crystalline phase changes or secondary phases, indicating the maintenance of the crystalline nature of hydroxyapatite after the grafting reaction [49–51] (Fig. 2b). These results confirmed that the modification only occurred selectively on the surface of Hap and did not alter the crystallinity, crystalline phase or intrinsic properties of V-Hap. The only exception was that a widened weak peak appeared around 22.5°, which was ascribed to the amorphous silica phase resulting from the hydrolysis condensation of VTES on the surfaces of Hap particles, further confirming the successful surface modification of V-Hap [51].

Fig. 2c shows TGA curves of Hap and V-Hap. The TGA curve for pure Hap showed a weight loss of 1.94% from room temperature to 150 °C, probably due to the evaporation of adsorbed H$_2$O. In the temperature range of 220–600 °C, the weight loss is 1.10%, which may be related to the decomposition of Hap [52]. For VTES-modified Hap, there was a weight loss of 2.38% from room temperature to 415 °C, which may be related to the removal of adsorbed H$_2$O and unreacted species. Then, there was a large decrease (8.92%) between 415 °C and 900 °C ascribed to the decomposition of the silane coupling agent. Next, the grafting efficiency was calculated using TGA, demonstrated that 8.26 wt% of VTES was coupled to Hap by comparing the differences of the total weight loss between V-Hap and Hap [29]. We then performed TEM to evaluate the morphology of Hap and V-Hap (Fig. S1). Both Hap and V-Hap demonstrated a rodlike morphology with no substantial difference. Moreover, the results of EDS revealed the presence of Ca, P, O, and Si in the V-Hap (Fig. S2a), among which Si originated from VTES, and Ca, P and O can be attributed to the Hap (Fig. S2b). These results suggested that V-Hap was prepared successfully.

3.2. Characterization of PS-DVB/V-Hap composites

Fig. 3a showed XRD patters of V-Hap, PS-DVB, and PS-DVB/V-Hap adsorbents with different weight percentages. The diffraction peaks of PS-DVB/V-Hap composites could only be indexed to PS-DVB and V-Hap, with no new peaks that could be possibly assigned to other phases,
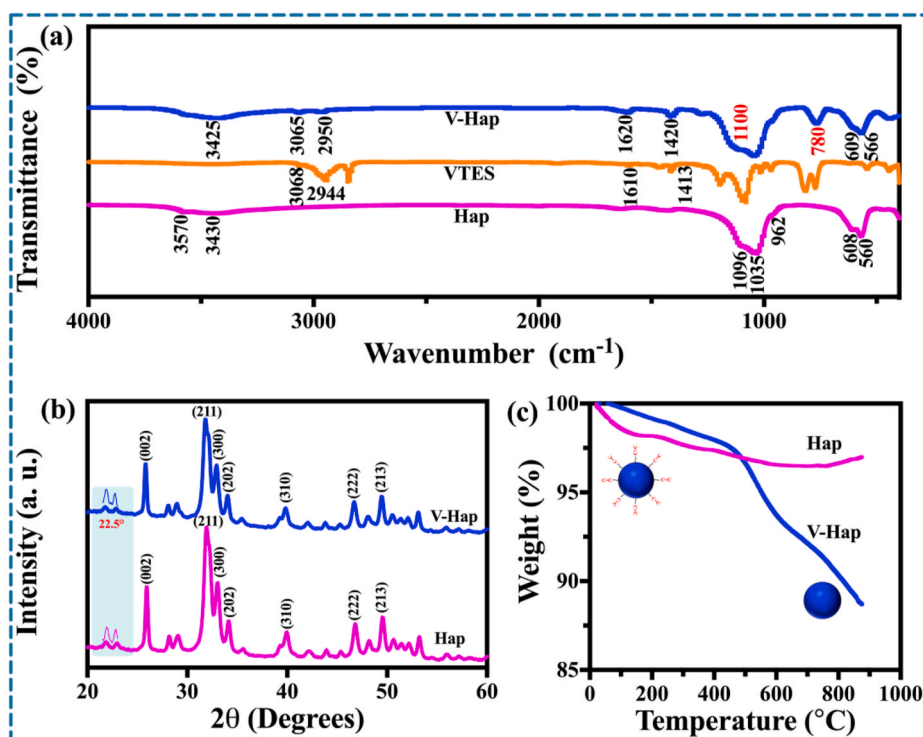
Fig. 2. Characterization of Hap and V-Hap. (a) FTIR spectra of V-Hap, VTES, and Hap. (b) XRD analysis of Hap and V-Hap with scanning rate of 10°/min in the 2θ ranges from 10° to 60° (Inset: the enlarged XRD patterns for the characteristic peak around 22.5°, amplification: 2 x.). (c) TGA plots of Hap and V-Hap with a temperature increase rate of 5 °C min^{-1}.

indicating the successful polymerization of V-Hap and PS-DVB. The XRD pattern of PS-DVB/V-Hap1 was similar to that of PS-DVB at a low content of V-Hap and showed no peaks indexed to V-Hap. As the content of V-Hap increased, the characteristic diffraction peaks at 25.96°, 31.77°, 32.90°, 34.05°, and 46.70°, corresponding to (0 0 2), (2 1 1), (3 0 0), (2 0 2), and (2 2 2) planes of V-Hap [53], became more clear and sharper from the improved crystallization. In addition, the characteristic diffraction peak of PS-DVB at 18° was observed in each PS-DVB/V-Hap composite, suggesting the co-existence of PS-DVB and V-Hap [54]. Compared with the pristine V-Hap, the diffraction peaks of PS-DVB/V-Hap composites slightly shifted to higher 2θ, which could be attributed to the compression from the contracting polymeric matrix through interfacial bonding [55].

This observation was supported by the FTIR results, and their spectra are shown in Fig. 3b. For PS-DVB, the absorption peak at 3438 cm^{-1} is due to the –OH stretching vibration of water adsorbed. The peaks at near 3086 and 3040 cm^{-1} are assigned to C–H stretching vibration of aromatic group [54]. The peaks at 2940 and 2857 cm^{-1} corresponded to the asymmetric and symmetrical stretching vibration of –CH$_2$–, respectively [56,57]. The peaks at 1704 and 1603 cm^{-1} are due to the skeleton vibration of the benzene ring [58]. The characteristic absorption peaks of saturated alkane methyl and methylene (1511-1358 cm^{-1}) can also be observed [59,60]. Also, the absorption peak at 989 cm^{-1} belongs to C=C stretching vibration of benzene ring [61]. Compared with V-Hap and PS-DVB, nanocomposites spectra showed typical peaks centered at 3040 and 2940 cm^{-1} that were attributed to the stretching vibrations of PS-DVB aromatic group and methylene group, respectively [61] as well as bands at 1098, 1039, 609, and 566 cm^{-1} related to V-Hap phosphate groups. Noteworthy, increasing V-Hap concentration in composites from 1 to 5 wt% resulted in a gradual increase of phosphate absorption band intensity. However, the peak at 566 cm^{-1} was not clearly seen, further indicating the low content of V-Hap in the nanocomposite. Moreover, the actual grafted amount of V-Hap was further supported by ICP-OES study. ICP-OES findings confirmed that 0.86 wt%, 1.53 wt%, 2.83 wt

%, 3.84 wt% and 5.75 wt% content of V-Hap in the filler in 1 wt%, 2 wt%, 3 wt%, 4 wt% and 5 wt% PS-DVB/V-Hap, respectively. Additionally, the TGA was also performed on pristine PS-DVB and the PS-DVB/V-Hap composite to confirm the thermal stability and V-Hap contents in organic-inorganic nanocomposites. As shown in Fig. S3, the weight losses of all the spheres were similar. Owning to the main-chain pyrolysis, a weight loss (75%) was observed from 350 °C to 485 °C in pristine PS-DVB. Compared with that of PS-DVB, the degradation of the nanocomposites appeared to be shifted to a higher temperature range. This indicated that there was a strong interaction between the polymer matrix PS-DVB and the V-Hap nanoparticles [62]. Also, actual ultimate V-Hap contents were estimated as 0.84 wt%, 1.74 wt%, 2.66 wt%, 3.87 wt% and 5.64 wt% compared with initial values of 1 wt%, 2 wt%, 3 wt%, 4 wt% and 5 wt%, respectively, consistent with results based on ICP-OES analysis. Taken together, these results indicated that V-Hap surface modification did not affect V-Hap crystal behavior in the PS-DVB matrix during polymerization.

Fig. S4 shows the surface morphology of various nanocomposite adsorbents with different V-Hap contents. All particles had a well-defined spherical morphology with a smooth surface and an average diameter of 300–500 μm, properties that would benefit a potential application to hemoperfusion. The cross-sections and surface micromorphology of the spheres were characterized by SEM images. As shown in Fig. S5, mesopores' cross-sections revealed that PS-DVB/V-Hap possessed penetrating mesoporous channels that were beneficial to the diffusion of guest molecules into the beads and increased the accessible adsorption sites. Well-formed structures with numerous mesopores on the surfaces of the spheres could be observed (Fig. 3c). Moreover, the nanocomposites with 3 wt% V-Hap exhibited the maximum pore porosity (Fig. S6). When the V-Hap content was further increased, the mesopore begun to decrease. This phenomenon may be due to aggregation in the polymer matrix resulting in a mesoporous structure that was destroyed.

To demonstrate the porous nature of prepared PS-DVB/V-Hap and
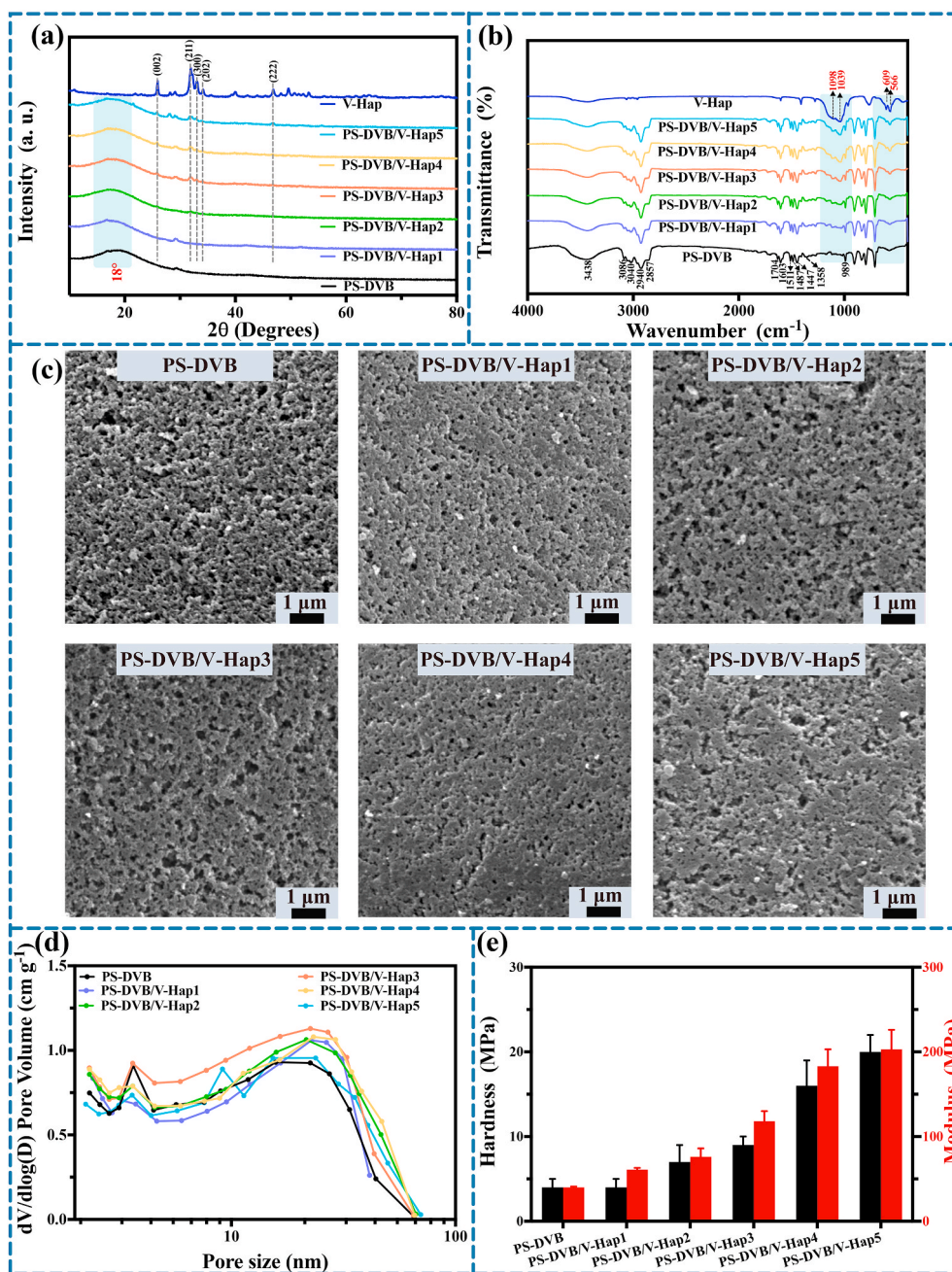
Fig. 3. Characterization of PS-DVB, PS-DVB/V-Hap and V-Hap. (a) XRD analysis of PS-DVB, PS-DVB/V-Hap, and V-Hap. (b) FTIR spectra of PS-DVB, PS-DVB/V-Hap, and V-Hap. (c) The morphologies of the surface pore structure of PS-DVB and PS-DVB/V-Hap. (d) PSDs by the BJH method of PS-DVB and PS-DVB/V-Hap. (e) Hardness and modulus of nanocomposite adsorbents.

PS-DVB, nitrogen adsorption-desorption isotherms were performed at 77 K. The isotherms exhibited a feature of type IV with a distinct hysteresis loop based on the IUPAC classification, indicating that the PS-DVB/V-Hap and PS-DVB adsorbents belong to typical mesoporous materials [63–65]. The hysteresis between the adsorption and desorption curves was caused by the adsorption and desorption processes being irreversible (Fig. S7). To further understand the porous structure of PS-DVB with different V-Hap contents, the size distribution of the pores and the textural properties of adsorbents are shown in Fig. 3d and Table S2, respectively. The size distribution of the pores (PSDs) showed similar patterns for PS-DVB/V-Hap and PS-DVB; PS-DVB/V-Hap3 had the most mesopores in the distribution and the largest mesopore volume, factors that would be beneficial to the diffusion of guest molecules into the adsorbents and would increase the accessible adsorption sites.

Moreover, in terms of the textural properties (Table S2), the PS-DVB/V-Hap3 adsorbents exhibited the maximum BET surface areas (S_{BET}) of 769.95 cm^2 g^{-1}, the largest total pore volume (T_p) of 2.1539 cm^3 g^{-1}, and BJH desorption average pore diameter (D_p) of 11.069 nm, indicating that the V-Hap nanoparticles had an advantage in the development of a mesoporous structure within the adsorbent. However, when the V-Hap content was further increased (>3 wt%), the obtained S_{BET}, T_p and D_p values begun to decrease. This phenomenon may have been due to excess V-Hap nanoparticles occupying part of the space in the mesopores and blocking a fraction of pores of PS-DVB adsorbents, which weakened the nano-effect [51]. The porous nature results were also in accordance with the SEM images.

Considering the pressure in the extracorporeal circuit, the mechanical properties of the spheres would be beneficial to maintaining their

dimensional stability. As shown in Fig. 3e, the mechanical strength enhanced with the increase of V-Hap content. In addition, the modulus and hardness of the pure PS-DVB were 40 ± 2 MPa and 4 ± 1 MPa, respectively, and those of the PS-DVB/V-Hap3 composite were increased to 118 ± 12 MPa and 9 ± 1 MPa, respectively. Furthermore, the loading-unloading nano-indentation curves also demonstrated a lower load on PS-DVB than on PS-DVB/V-Hap (Fig. S8). Considering that a bilirubin adsorbent requires an abundant mesopore structure and excellent mechanical strength, the PS-DVB/V-Hap3 was selected as the representative sample for further characterization. HRTEM was used to investigate the internal nano-scaled structure of PS-DVB/V-Hap3. As presented in Fig. S9, the expected lattice fringe with interplanar spacing (d values) of

0.3077 and 0.1846 nm, corresponding to the (2 1 0) and (2 1 3) planes of hexagonal Hap ($d_{210} = 0.3080$ and $d_{213} = 0.1841$ nm, JCPDS No.9–432) [66–68], respectively, further demonstrated that V-Hap was successfully added to the PS-DVB/V-Hap, in good agreement with the XRD analysis, while there was no such pattern observed in PS-DVB (Fig. 3a). More importantly, EDS was performed on the PS-DVB/V-Hap3 to further evaluate the adsorbent's elemental characteristics. Compared with the result of PS-DVB (Fig. S10), the appearance of an even distribution of Ca, P, and Si elements in the results of PS-DVB/V-Hap3 further confirmed the homogenous structure within the organic-inorganic copolymer. Together, the above results suggested the successful synthesis of PS-DVB/V-Hap. Notably, there were three points that should be
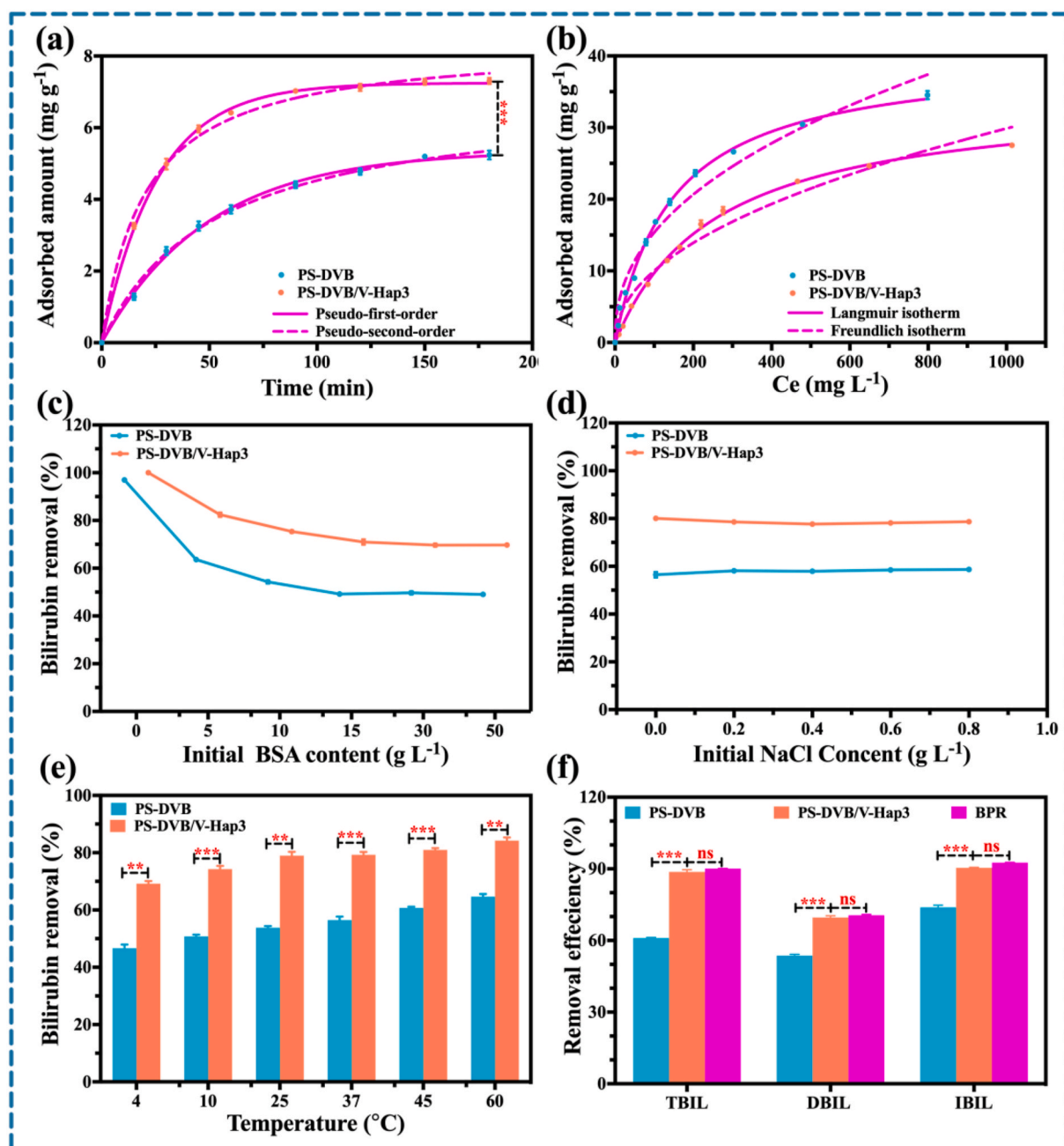
Fig. 4. *In vitro* adsorption experiments. (a) Adsorption kinetics model of bilirubin onto PS-DVB and PS-DVB/V-Hap3 (T = 37 °C, $C_{bilirubin}$ = 150 mg L^{-1}). (b) Bilirubin adsorption isotherms for PS-DVB and PS-DVB/V-Hap3 (T = 37 °C, t = 2 h). (c–e) Effect of microenvironment on adsorption of bilirubin for PS-DVB and PS-DVB/V-Hap3. (c) Effect of albumin in the adsorption medium ($C_{bilirubin}$ = 150 mg L^{-1}, T = 37 °C, t = 2 h). (d) Effect of ionic strength of the solution ($C_{bilirubin}$ = 150 mg L^{-1}, C_{BSA} = 15 g L^{-1}, T = 37 °C, t = 2 h). (e) Effect of temperature ($C_{bilirubin}$ = 150 mg L^{-1}, C_{BSA} = 15 g L^{-1}, T = 37 °C, t = 2 h). (f) Adsorption capacity of PS-DVB, PS-DVB/V-Hap3, and BBR in plasma of patients with hyperbilirubinemia *in vitro* (T = 37 °C, t = 2 h). (Mean $\pm$ SD, n = 3 for each group), **p < 0.01, ***p < 0.001; ns.: Not significant.

emphasized: (1) The adding of V-Hap had no effect on the morphology of adsorbent. (2) The obtained PS-DVB/nHAp3 had the highest pore volume and most abundant mesoporous structure, making it the most efficient for removal of bilirubin. (3) The as-prepared PS-DVB/nHAp had an optimized mechanical performance, suggesting that it could be safely used for hemoperfusion.

3.3. In vitro adsorption experiments

The effect of PS-DVB adsorbents with different V-Hap content (0, 1, 2, 3, 4, and 5 wt%) on bilirubin adsorption capacity was studied; the results are shown in Fig. S11. The nanocomposite has the largest adsorption amount of bilirubin when the V-Hap content was 3 wt% (7.4 mg g^{-1}), and the adsorption rate was 79.26 $\pm$ 1.02%; this value was consistently higher than that the of PS-DVB (56.49 $\pm$ 1.18%) (p < 0.0001). Additionally, there was an increase in the adsorption capacity of bilirubin with an increase in the V-Hap content from 0 to 3 wt%. However, further increase in the V-Hap content from 3 to 5 wt% resulted in a decrease of the bilirubin removal efficiency. This may be due to 3 wt % PS-DVB/V-Hap adsorbent having the most developed mesoporous structure (Fig. 3c), the largest pore size, and largest pore volume (Table S2). The bilirubin is adsorbed mainly by hydrophobic interactions, resulting in an enhanced effective bilirubin removal. Therefore, PS-DVB/V-Hap3 was employed as the optimal adsorbent material for the application of the treatment to hyperbilirubinemia.

3.3.1. Assessment of adsorption mechanism

The study of adsorption kinetics described the solute uptake rate. Therefore, we assessed the adsorption kinetics of the adsorbent from initial to adsorption equilibrium. Fig. 4a and Table S3 show the kinetics of adsorption of bilirubin by the adsorbents in the simulated serum. The adsorption was initially quite rapid during the first 30 min, and the adsorption then slowed, reached equilibrium within 2 h. The maximum amount of bilirubin adsorbed by PS-DVB/V-Hap3 is about 7.40 mg g^{-1}, which was significantly higher than that of PS-DVB (5.38 mg g^{-1}). Rapid adsorption during the initial minutes was due to a large number of vacant adsorption sites existing on the surface of composites. In order to further examine the controlling mechanisms of adsorption such as mass transfer and chemical reactions, pseudo-first-order and pseudo-second-order kinetics were utilized to model the experimental data [69,70]. The coefficient of determination R^2 of the pseudo-first-order model was higher than that of the pseudo-second-order model, indicating a better fit with the pseudo-first-order and suggesting that the pseudo-first-order equation was more suitable for describing the adsorption process (Table S4). These results also confirmed that the adsorption efficiency was proportional to the number of free sites and that hydrophobic forces may play a critical role in the adsorption of bilirubin using composite beads.

The adsorption isotherms were used to describe the adsorption progress to investigate the mechanisms of adsorption and to estimate the maximum adsorption capacity of adsorbents, as depicted in Fig. 4b and Table S5. According to the Giles's classification of liquid adsorption isotherms, the shapes of isotherms of adsorption of bilirubin onto two adsorbents were H-2 type [71], indicating that both had the same mechanism of adsorption for bilirubin. An H-2 type adsorption isotherm suggested that bilirubin molecules were adsorbed in the mesopores of adsorbents. This behavior is due to the relationship between the pore structure and molecular size of bilirubin. To our knowledge, the area per of bilirubin molecule is 0.74 nm^2, and its molecular size is estimated to be 1–2 nm [72,73]. In simulated serum, free bilirubin can bind to albumin with an association constant of 9.5 $\times$ 10^7 M^{-1} to form indirect bilirubin with hydration diameters of about 7 nm [74]. Meanwhile, the adsorbents had mesopores with diameters of 5–20 nm. Therefore, the bilirubin molecules could access and be adsorbed in the mesopores of adsorbents, resulting in the acceleration of adsorption due to the adsorption potential field of the mesopores. Moreover, two well-known

theoretical models, i.e., Langmuir and Freundlich models, were used to fit the experimental data [69,75,76]. Nonlinear fitting was performed (Fig. 4b) with the relevant parameters calculated from the two models listed in Table S6. According to the maximum adsorption amount, R^2 values, and fitting curves, the adsorption of bilirubin by the two adsorbents was typical monolayer adsorption in the simulated serum. The maximum adsorption capacities from Langmuir model for PS-DVB and PS-DVB/V-Hap3 were 34.71 and 40.27 mg g^{-1}, respectively. Compared with PS-DVB, the larger S$_{BET}$, D$_p$ and T$_p$ of PS-DVB/V-Hap3 may further facilitate adsorbate diffusion processes inside polymer particles, which favors a solute-solute interaction for protein-binding bilirubin (molecular size: 7 nm) according to the capillary condensation theory [77]. This is in agreement with some earlier reports [78].

3.3.2. The effect of microenvironment factors on the adsorption of bilirubin

The effect of albumin concentration, ionic strength and temperature on the adsorption of bilirubin are illustrated in Fig. 4c–e and Tables S7–S9. The concentration of albumin is one of the most important properties in the adsorption studies; due to the albumin being a natural vector of bilirubin, a bilirubin-albumin complex can be formed in blood. The molecular weight of albumin is 66 KDa, and the protein contains two strong bilirubin-binding sites and ten comparatively weak binding sites. The bilirubin sorption decreased with the increasing of concentration of albumin (Fig. 4c and Table S7). This result could be attributed to two factors. On the one hand, the presence of excess albumin could conjugate with bilirubin [79], resulting in a decrease in the amount of free bilirubin. On the other hand, competition between the albumin and the adsorbents for binding to the bilirubin decreased the number of collisions between bilirubin and adsorbents. However, there was no obvious change in the adsorbed amount when the concentration of albumin reaches about 15 g L^{-1}. The reason may be that the conjugate BSA-bilirubin reach a saturated adsorption state. Additionally, the concentration of albumin had a relatively small effect on the adsorption capacity of PS-DVB/V-Hap3, compare with the PS-DVB. This can be attributed to the addition of V-Hap enhancing the adsorption selectivity toward bilirubin against albumin interference. Thus, the initial concentration provides an important driving force to overcome all mass transfer resistances between the aqueous and solid phases.

Generally, various salts ions are present in human plasma. The salts lead to high ionic strength, which may affect the adsorption onto adsorbents (Fig. 4d and Table S8). The adsorb amounts of PS-DVB and PS-DVB/V-Hap3 at varying concentrations of NaCl (0–0.8 M) showed no significant increases, indicating that the prominent adsorption mechanism between PS-DVB/V-Hap3 and bilirubin is still a hydrophobic interaction, and that PS-DVB/V-Hap3 adsorption toward bilirubin was stable against salts interference. The temperature is also important for the adsorption performances. As shown in Fig. 4e and Table S9, an increase in temperature from 4 to 60 °C enhanced the remove efficiency significantly. This was mainly due to the increased temperature making the bilirubin molecules form more intermolecular H-bonds, resulting in an increase of their hydrophobicity and thus an increase in the hydrophobic interaction between adsorbate and adsorbent. In addition, the rate of diffusion of the adsorbate molecules across the external boundary layer and in the internal pores of the adsorbent particle can be enhanced with increasing temperature, owing to the decrease in the viscosity of the solution for high-temperature suspensions [80]. Taken together, these results indicated that PS-DVB/V-Hap3 had higher absorbability of bilirubin.

In order to further evaluate the adsorbent, we tested the adsorption capacity of PS-DVB/V-Hap3 in the plasma of patients with hyperbilirubinemia in vitro, and a commercial bilirubin adsorbent (BPR, made in japan) was used as a positive control. As shown in Fig. 4f and Table S10, the absorption capacity for TBIL, DBIL and IBIL of the PS-DVB/V-Hap3 and BPR was equal, while PS-DVB/V-Hap3 had significantly higher adsorption rates than PS-DVB. However, BPR is a typical anion exchange resin, it can only be used for plasma perfusion. PS-DVB/

V-Hap3 is designed on the basis of whole blood perfusion, which does not rely on plasma separator and can be used in a safer, more convenient and cost-reducing way.

3.4. Biosafety assessment of PS-DVB/V-Hap3

As a hemoperfusion adsorbent has direct contact with blood or plasma, good biocompatibility is necessary. Unexpected leukopenia, hemolysis, and thrombocytopenia during hemoperfusion treatment suggest poor hemocompatibility of blood-contacting biomaterials. Since abnormal hemolysis leads to hemolytic anemia (HA), jaundice, fatigue, cholelithiasis, pulmonary hypertension, and renal dysfunction, hemolysis ratios are important to confirm the safety and feasibility of adsorbents [12]. As shown in Fig. 5a, compared with PS-DVB (2.8%), PS-DVB/V-Hap3 showed lower hemolysis rates (1.3%); this not only met the requirements of the hemolysis experiment of applied materials (ASTM, F756-2008) but also indicated better blood compatibility [81]. By contrary, BPR has a higher hemolysis rate (19.45%). Thus, PS-DVB/V-Hap3 can be classified as a nonhemolytic nano-composite adsorbent clinical hemoperfusion adsorption material.

Moreover, blood coagulation, including analyses of activated partial thromboplastin time (APTT), thrombin time (TT), prothrombin time (PT), and the fibrinogen (FIB), was performed to study the coagulant property (Fig. 5b). The APTT and TT can assess the antithrombogenicity of the samples *in vitro*; PT can confirm the exogenous coagulation ability, while the adsorption of FIB was used to evaluate the pro-coagulant activity. Compared with the control group of PPP, the values of APTT, TT, PT and FIB for PS-DVB/V-Hap3 and PS-DVB showed no significant reductions, suggesting that PS-DVB/V-Hap3 caused little whole blood coagulation.

Furthermore, blood cell differential counts were measured to study the overall effect of adsorbents on whole blood. As shown in Fig. 5c, there were no obvious difference among control (BPR), PS-DVB, and PS-DVB/V-Hap3 groups for white blood cells (WBC), red blood cells (RBC), or hemoglobin (HGB). It is worth mentioning that the decreased rate of platelet (PLT) for PS-DVB/V-Hap3 was lower (only 8.2%) than in the control group (30.2%). Additionally, the concentrations of major proteins, ions, and other coagulation-related compounds showed no significant decreases when compared to the control groups, indicating that the spheres did not induce any nonspecific adsorption (Table S11). These results demonstrate that PS-DVB/V-Hap3 spheres had better blood compatibility, a result that provides the foundation for safe treatment in whole blood.

Lastly, the cytotoxicity test results (Fig. 5d) showed that the relative increase rate of cells in the positive control group was 26.52%, in accordance with the evaluation criteria. The relative cell proliferation rates were 86.75% and 94.29% for PS-DVB and PS-DVB/V-Hap3, respectively, conforming the nontoxicity and better biocompatibility of PS-DVB/V-Hap3. Taken together, these results demonstrated that the PS-DVB/V-Hap3 could be applied in direct contact with blood, and that it is feasible and safe as a clinical hemoperfusion adsorption material.

3.5. Extracorporeal whole blood cleaning in living animals

3.5.1. Establishment of hyperbilirubinemia model

A hyperbilirubinemia model can be constructed by bile duct ligation [82,83] (Fig. 6a). The skin, lips, and eyeballs turned yellow in bile duct ligation pigs after seven days (Figs. S12a and S12b). Meanwhile, the plasma bilirubin levels before and after modeling were analyzed (Fig. 6b). The results showed the TBIL, DBIL, and IBIL increased significantly from 1.28 ± 0.50, 0.85 ± 0.38 and 0.44 ± 0.27 to 139.47 ± 9.36, 119.32 ± 6.77 and 20.90 ± 3.56 μmol L^{-1}, respectively, indicating
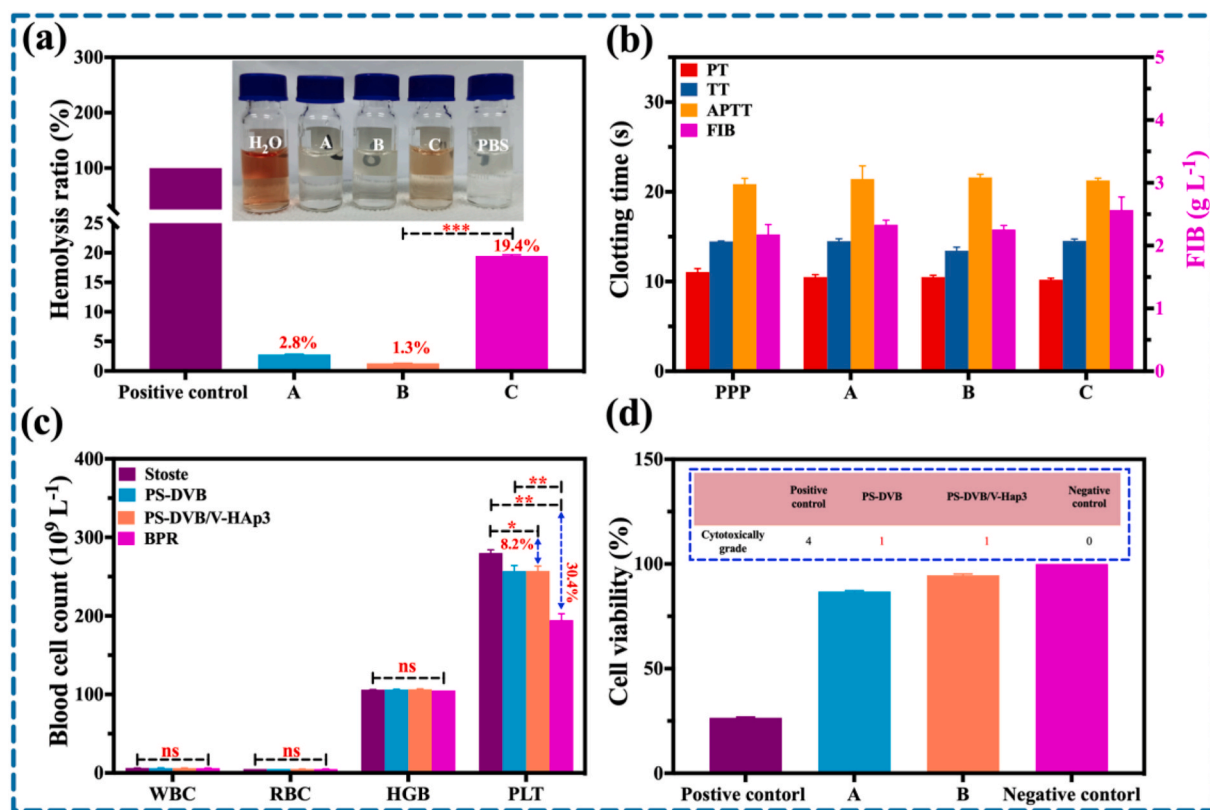
Fig. 5. Blood compatibility and biocompatibility evaluation of the adsorbents. (a) Hemolysis rate results for control groups and adsorbents (Inset shows a digital photo of red blood cells incubated with different samples.). (b) TT, APTT, PT and FIB in PPP after incubation with different adsorbents. (c) Comparison of the blood cell count for normal whole blood and the blood after incubating with adsorbents. (d) The cell viability of NIH3T3 cells of adsorbents by CCK-8 assay (Inset shows the cytotoxically grade.). A: PS-DVB, B: PS-DVB/V-Hap3 and C: BPR (Mean $\pm$ SD, n = 6 for each group), $*p < 0.05$, $**p < 0.01$, $***p < 0.001$; ns.: Not significant.
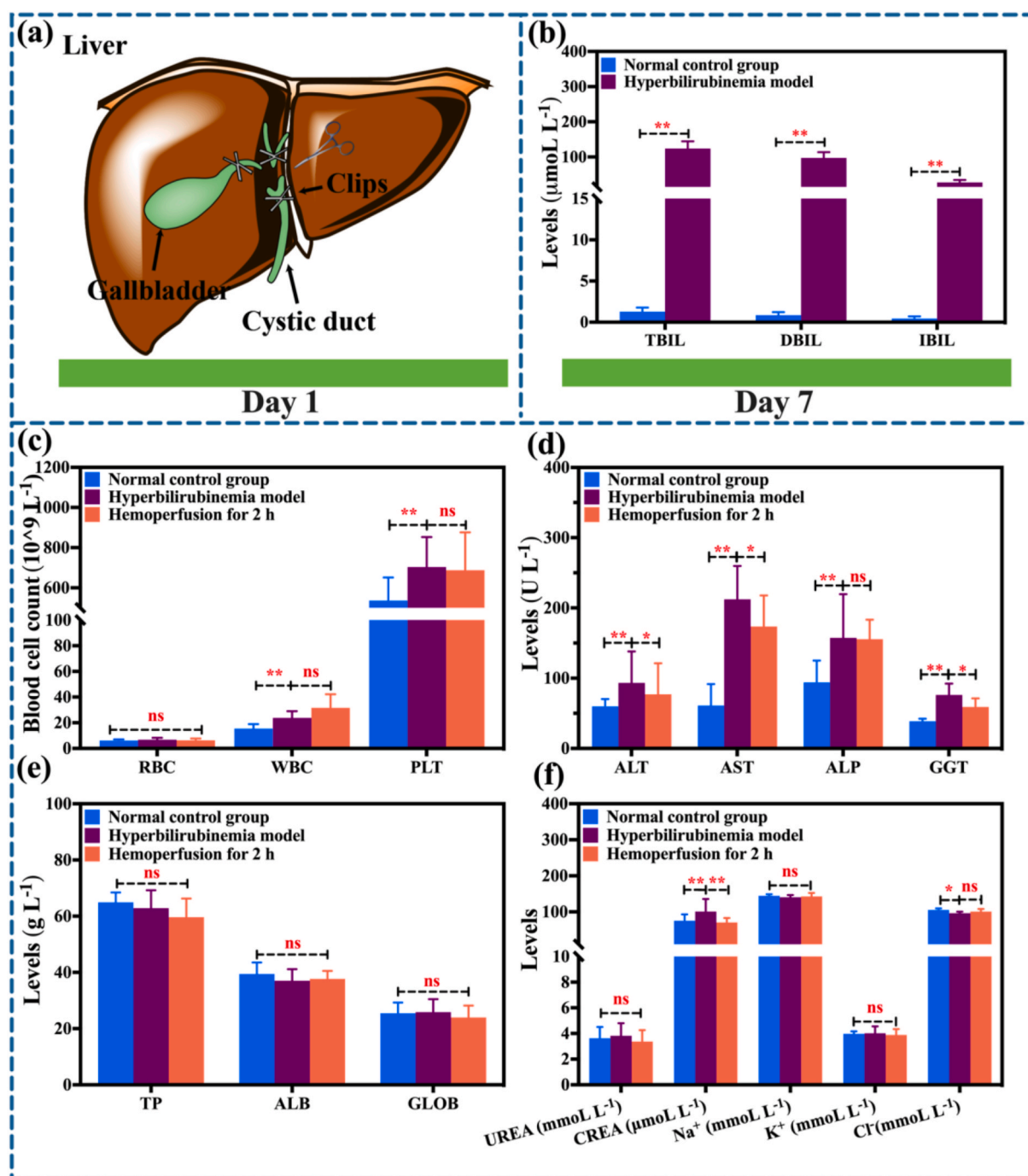
Fig. 6. (a) A schematic of the fabrication of bile duct ligation. (b) The levels of TBIL, DBIL, and IBIL in pigs before and after model establishment. (c–f) The parameters of blood routine examination, liver function, proteins, and renal function were analyzed before and after the 2-h hemoperfusion process. (Mean ± SD, n = 6 for each group), *p < 0.05, **p < 0.01; ns.: Not significant.

a successful model (Fig. 6b). Moreover, the routine blood results of the models suggested that a 53.16% increased of WBC may have been caused by the inflammatory response after the operation to resist infection, and a 31.16% increased of PLT may have been due to decreased or refused diet and inadequate water intake after ligation (Fig. 6c). The concentration of RBC remained constant; there was no significant difference, i.e., no indication of dehydration. The liver function results of pigs with hyperbilirubinemia suggested the levels of alanine aminotransferase (ALT), aspartate aminotransferase (AST), alkaline phosphatase (ALP) and γ-glutamyl transpeptidase (GGT) were significantly higher than normal, indicating that the pigs had clear liver

dysfunction (Fig. 6d). Moreover, there was no significant differences in total protein (TP) or globulin (GLOB) before and after the model (p > 0.05); and a 5.1% reduction in concentration of albumin (ALB) suggested that it may have been due to liver function injury and animals eating less or refusing to eat after surgery (Fig. 6e). The comprehensive assessment the parameters of kidney function and electrolyte indexes (Fig. 6f) showed the concentrations of creatinine (CREA) increased by 25.86% and Cl⁻ decreased by 8.57%, both of which were statistically significant. Taken together, the results further confirmed the successful induction of hyperbilirubinemia.

3.5.2. Toxicity in vivo during hemoperfusion in pigs

The blood count is the main safety index for evaluating the blood compatibility of biomaterials. After treatment, the levels of WBC increased slightly ($p > 0.05$) (Fig. 6c), which might be a transient increase caused by the contact between blood and adsorbent but returned to pre-treatment level by 24 h after hemoperfusion (Fig. S13). In addition, the levels of PLT decrease slightly during hemoperfusion, without significant difference ($p > 0.05$). These results indicated that PS-DVB/V-Hap3 did not cause remarked changes in the numbers of various blood cells and thereby demonstrating its low toxicity. The statistical results for ALT, AST, ALP, and GGT are shown in Fig. 6d. Notably, after treatment with hemoperfusion for 2 h, the levels of ALT, AST, and GGT were significantly decreased, while the level of ALP decreased slightly, indicating that using the PS-DVB/V-Hap3 hemoperfusion apparatus could potentially reduce liver damage and improve clinical outcomes. The effect on proteins is also an important indicator in hemoperfusion for bilirubin. The levels of proteins were slightly decreased during hemoperfusion, possibly due to physical adsorption of the adsorbent, but this decline is within the range of clinical acceptance and does not make a significant change of blood components after treatment ($p > 0.05$) (Fig. 6e). Furthermore, except for the observed change in CREA, there were no significant changes in renal function during 2 h hemoperfusion (Fig. 6f). The decrease of CREA might primarily result from the hemodilution caused by fluid infusion [84].

The vital signs were further evaluated during hemoperfusion. The animal's physiology (respiratory and heartbeat rates) was monitored during the irrigation process to assess whether the basic conditions of the animals were stable, as shown in Fig. 7a and b. The physiological responses were basically stable and did not show sudden rises and/or lows, and the procedure did not cause adverse reactions such as heart failure, respiratory failure, or arrhythmia. In addition, due to the different tolerance of individual animals to anesthesia, the statistical deviation was large. Considering the characteristics of high coagulation in pigs, the first dose of anticoagulation was given at the beginning of the experiment; this was higher than the clinical dosage of humans. The anticoagulant test results are shown in Fig. 7c. The results indicated that the PT increased when the hemoperfusion lasted for 2 h but recovered to normal levels at 24 h. This is most probably because heparin sodium could not be completely metabolized in the body during the treatment of 2 h. The levels of FIB remained substantially constant, indicating that there were no significant changes after treatment. The digital photos of hemoperfusion apparatus are shown in Fig. 7d. There was no substantial difference between before and after hemoperfusion for the spheres in the apparatus, and no obvious blood clotting could be observed on the inside wall of the apparatus after treatment; this also indicated that PS-DVB/V-Hap3 shows little blood adherence effect.

3.5.3. Evaluation of effectiveness in hemoperfusion

To test the whole blood-cleaning capability of the TBIL, DBIL and IBIL *in vivo*, blood was taken from the carotid artery and returned to the jugular veins of living, anesthetized pigs using PS-DVB/V-Hap3 hemoperfusion apparatus (Fig. 8a–c). Furthermore, the TBIL, DBIL and IBIL levels of the therapeutic group decreased drastically, from 139.47 ± 9.36, 119.32 ± 6.77 and 20.90 ± 3.56 to 93.25 ± 8.17, 81.97 ± 8.02 and 9.23 ± 2.33 μmoL L^{-1}, respectively, in the hyperbilirubinemia pig's whole blood circulation for the entire 2 h treatment period. We further confirmed removal efficiencies of $32.93\% \pm 9.52\%$, $31.3\% \pm 9.09\%$ and $55.5\% \pm 11.04\%$ for TBIL, DBIL and IBIL, respectively (Fig. 8d–f). Combining the low toxicity with the efficiency of PS-DVB/V-Hap3, the results suggested that the nanocomposite materials could be a new type of hemoperfusion adsorbent for bilirubin removal from whole blood directly in clinical therapy for hyperbilirubinemia.
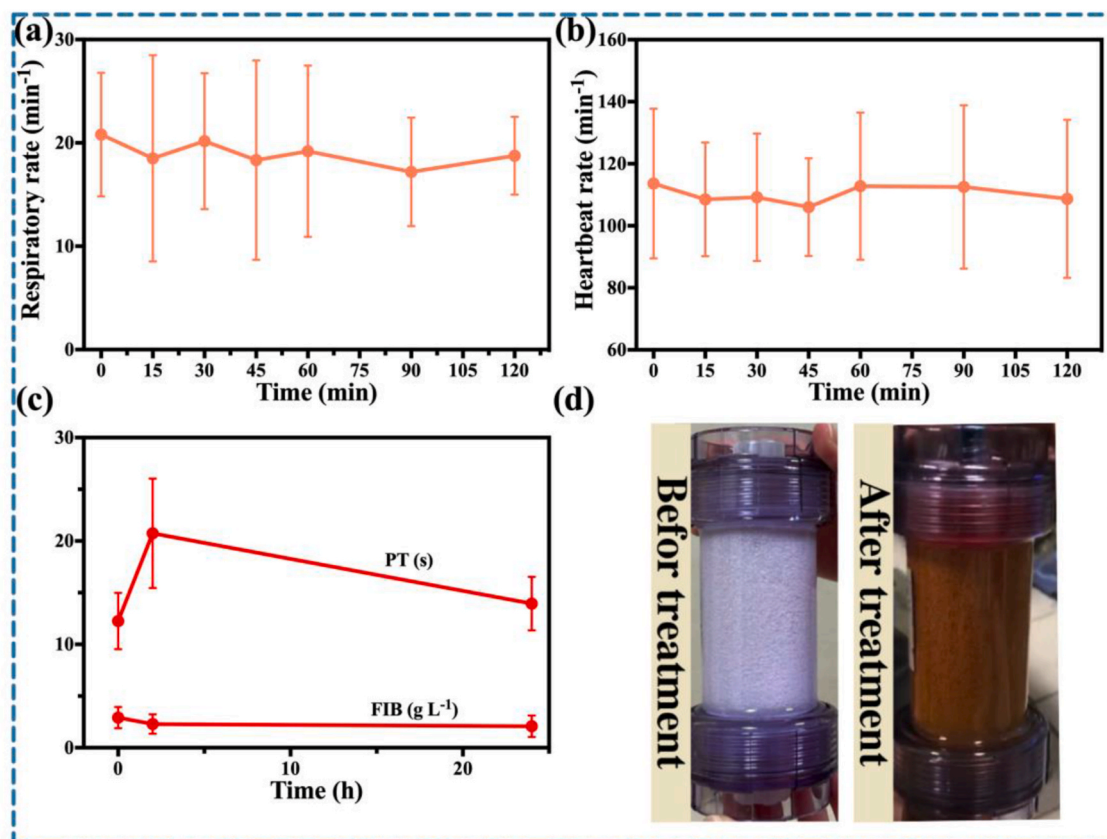
Fig. 7. The physicochemical properties before and after hemoperfusion. (a) Respiratory rates. (b) Heartbeat rates. (c) Coagulation assays. (d) Digital photos of spheres in the apparatus before and after hemoperfusion. (Mean $\pm$ SD, n = 6 for each group).
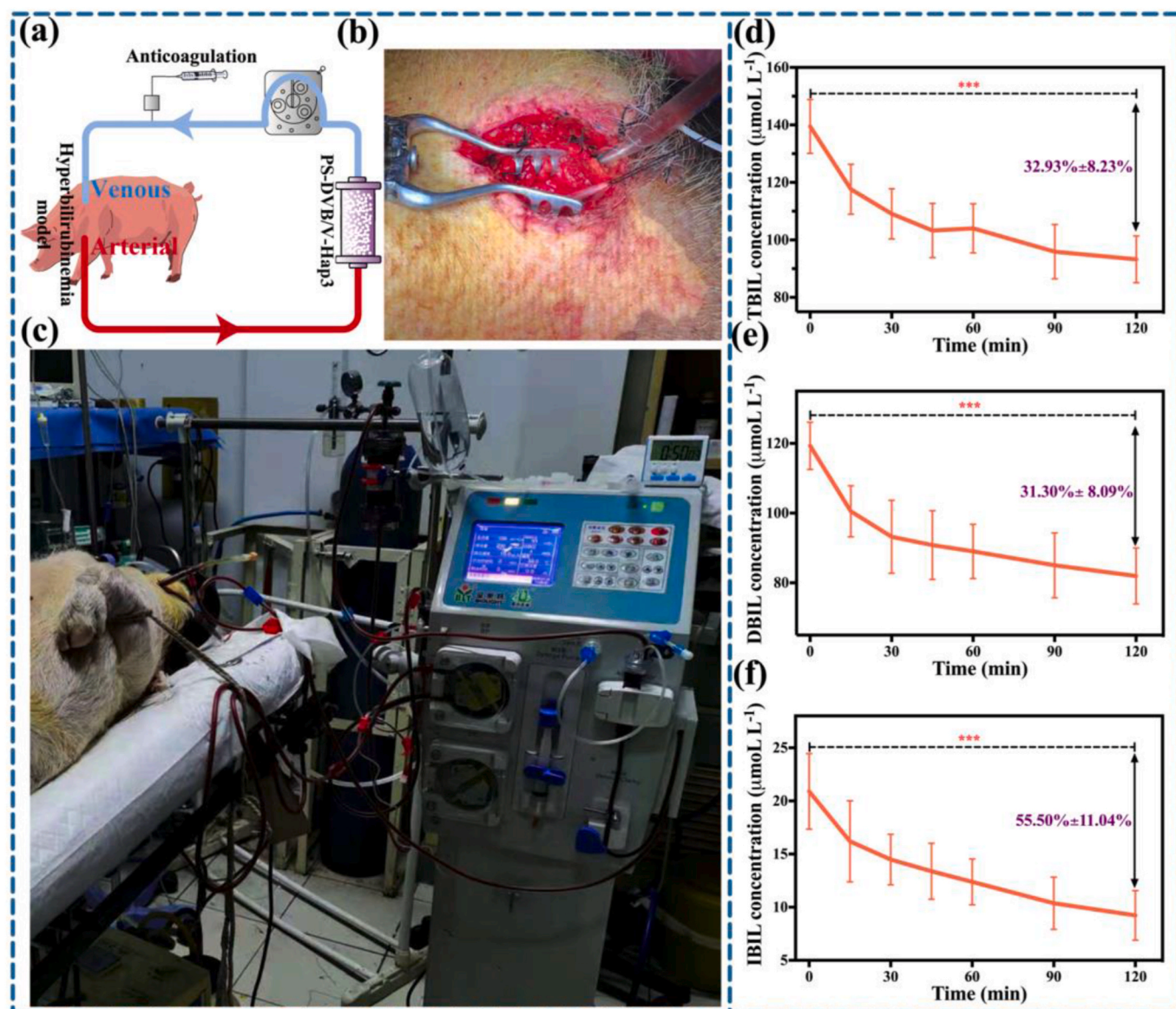
Fig. 8. *In vivo* blood cleansing using the hemoperfusion device in a pig hyperbilirubinemia model. (a) A schematic of whole blood hemoperfusion. (b) Venous cannula of pigs. (c) Photograph of the experimental animal setup for extracorporeal blood cleansing. (d–f) Depletion of TBIL, DBIL and IBIL levels and clearance rates for the entire 2-h treatment period, respectively. (Mean $\pm$ SD, n = 6 for each group), ***p < 0.001.

4. Conclusion

In summary, we have successfully developed a novel organic-inorganic nanocomposite (PS-DVB/V-Hap3) with high efficiency for hyperbilirubinemia therapy by bilirubin removal directly from whole blood. The nanocomposite spheres possessed large specific surface area, high pore volume, and an abundant mesoporous structure that resulted in a high adsorption capacity for bilirubin. Due to the improved interfacial bonding between V-Hap and PS-DVB through the formation of a covalent co-crosslinked network, the nanocomposite also displayed significantly enhanced mechanical properties. Surprisingly, the modulus and hardness of PS-DVB/V-Hap3 reached 9 $\pm$ 1 MPa and 118 $\pm$ 12 MPa, respectively. These high values mean that PS-DVB/V-Hap3 was much more suitable for hemoperfusion applications than PS-DVB. More importantly, the V-Hap endowed PS-DVB spheres with excellent blood compatibility and biocompatibility. Last but not least, *in vivo* hyperbilirubinemia pig model experiments further confirmed that the adsorbent had significant advantages regarding biosafety performance as well as absorptive property using whole blood. After 2 h hemoperfusion, the

TBIL, DBIL, and IBIL levels of the therapeutic group decreased from 139.47 $\pm$ 9.36, 119.32 $\pm$ 6.77 and 20.90 $\pm$ 3.56 to 93.25 $\pm$ 8.17, 81.97 $\pm$ 8.02 and 9.23 $\pm$ 2.33 μmol L^{-1}, respectively. Taken together, these results suggested that PS-DVB/V-Hap3 is an effective, safe, and cost-effective adsorbent, one that could be used in a commercial hemoperfusion column to treat hyperbilirubinemia. The new material could surmount the defects of extant techniques and finally improve the clinical outcomes of patients with hyperbilirubinemia.

Data availability

The data used in the present study are available from the corresponding author on reasonable request.

CRediT authorship contribution statement

Yamin Chai: Investigation, Methodology, Validation, Writing – original draft. **Zhuang Liu:** Responsible for the assistance of animal experiment. **Yunzheng Du:** Responsible for the synthesis of V-Hap.

Lichun Wang: Responsible for parts of cell experiments. **Jinyan Lu:** Responsible for the assistance of animal experiments. **Qian Zhang:** Methodology, Responsible for the assistance of animal experiments. **Wenyan Han:** Data curation, Responsible for the guidance of animal experiment. **Tingting Wang:** Data curation. **Yameng Yu:** Data curation. **Lisha Sun:** Responsible for the assistance of sample testing. **Lailiang Ou:** Conceptualization, Supervision, Project administration, Funding acquisition, Methodology, Writing – original draft, Writing – review & editing.

Declaration of competing interest

The authors declare that they have no known competing financial interests or personal relationships that could have appeared to influence the work reported in this paper.

Acknowledgements

Appendix A. Supplementary data

Supplementary data to this article can be found online at https://doi.org/10.1016/j.bioactmat.2021.05.017.

References

[1] M. Amato, Mechanisms of bilirubin toxicity, Eur. J. Pediatr. 154 (4) (1995) S54–S59, https://doi.org/10.1007/BF02191507.

[2] R. Bonnett, J. Davies, M. Hursthouse, G. Sheldrick, The structure of bilirubin, Proc. R. Soc. Lond. Ser. B Biol. Sci. 202 (1147) (1978) 249–268, https://doi.org/10.1098/rspb.1978.0066.

[3] X. He, D. Carter, Atomic structure and chemistry of human serum albumin, Nature 358 (6383) (1992) 209–215, https://doi.org/10.1038/358209a0.

[4] T. Morimoto, M. Matsushima, N. Sowa, K. Ide, K. Sawanishi, Plasma adsorption using bilirubin-adsorbent materials as a treatment for patients with hepatic failure, Artif. Organs 13 (5) (1989) 447–452, https://doi.org/10.1111/j.1525-1594.1989.tb01556.x.

[5] J. Patel, A. Taneja, D. Niccum, G. Kumar, E. Jacobs, R. Nanchal, The association of serum bilirubin levels on the outcomes of severe sepsis, J. Intensive Care Med. 30 (1) (2015) 23–29, https://doi.org/10.1177/0885066613488739.

[6] J. Martinez, H. Garcia, L. Otheguy, G. Drummond, A. Kappas, Control of severe hyperbilirubinemia in full-term newborns with the inhibitor of bilirubin production Sn-mesoporphyrin, Pediatrics 103 (1) (1999) 1–5, https://doi.org/10.1542/peds.103.1.1.

[7] J. Feng, M. Li, Q. Wei, S. Li, S. Song, Z. Hua, Unconjugated bilirubin induces pyroptosis in cultured rat cortical astrocytes, J. Neuroinflammation 15 (1) (2018) 1–10, https://doi.org/10.1186/s12974-018-1064-1.

[8] T. Hansen, Mechanisms of bilirubin toxicity: clinical implications, Clin. Perinatol. 29 (4) (2002) 765–778, https://doi.org/10.1016/S0095-5108(02)00053-2.

[9] S. Sideman, L. Mor, L. Fishler, I. Thaler, J. Brandes, Bilirubin removal by sorbent hemoperfusion from jaundiced blood, Artif. Liver Supp. (1981) 103–109, https://doi.org/10.1007/978-3-642-96629-3_15.

[10] S. Sideman, L. Mor, M. Mihich, D. Mordohovich, S. Lupovich, J. Brandes, M. Zeltzer, Resin hemoperfusion for unconjugated bilirubin removal, Contrib. Nephrol. 29 (1982) 90–100, https://doi.org/10.1159/000406181.

[11] M. Usami, H. Nomura, S. Nishimatsu, H. Shiroiwa, H. Kasahara, Y. Takeyama, Y. Saitoh, In vivo and in vitro evaluation of bilirubin removal in postoperative hyperbilirubinemia patients, Artif. Organs 19 (1) (1995) 102–105, https://doi.org/10.1111/j.1525-1594.1995.tb02254.x.

[12] R. Zhao, T. Ma, F. Cui, Y. Tian, G. Zhu, Porous aromatic framework with tailored binding sites and pore sizes as a high-performance hemoperfusion adsorbent for bilirubin removal, Adv. Sci. 7 (23) (2020), https://doi.org/10.1002/advs.202001899, 2001899.

[13] J. Chen, G. Cheng, Y. Chai, W. Han, W. Zong, J. Chen, C. Li, W. Wang, L. Ou, Y. Yu, Preparation of nano-CaCO₃/polystyrene nanocomposite beads for efficient bilirubin removal, Colloids Surf. B Biointerfaces 161 (2018) 480–487, https://doi.org/10.1016/j.colsurfb.2017.11.017.

[14] S. Nakaji, N. Hayashi, Bilirubin adsorption column medisorba BL-300, Ther. Apher. Dial. 7 (1) (2003) 98–103, https://doi.org/10.1046/j.1526-0968.2003.00007.x.

[15] M. K van Gelder, J.A. Jong, L. Folkertsma, Y. Guo, C. Blüchel, M.C. Verhaar, M. Odijk, C.F. Van Nostrum, W.E. Hennink, K.G. Gerritsen, Urea removal strategies for dialysate regeneration in a wearable artificial kidney, Biomaterials 234 (2020), https://doi.org/10.1016/j.biomaterials.2019.119735, 119735.

[16] X. Yang, S. Xin, Y. Zhang, T. Li, Early hemoperfusion for emergency treatment of carbamazepine poisoning, Am. J. Emerg. Med. 36 (6) (2018) 926–930, https://doi.org/10.1016/j.ajem.2017.10.048.

[17] G. Adani, D. Lorenzin, G. Currò, M. Sainz-Barriga, C. Comuzzi, V. Bresadola, C. Avellini, U. Baccarani, Selective bilirubin removal by plasma treatment with Plasorba BR-350 for early cholestatic graft dysfunction, Transplant. Proc. 39 (6) (2007) 1904–1906, https://doi.org/10.1016/j.transproceed.2007.05.010.

[18] B. Meijers, P. Verhamme, F. Nevens, M. Hoylaerts, B. Bammens, A. Wilmer, J. Arnout, Y. Vanrenterghem, P. Evenepoel, Major coagulation disturbances during fractionated plasma separation and adsorption, Am. J. Transplant. 7 (9) (2007) 2195–2199, https://doi.org/10.1111/j.1600-6143.2007.01909.x.

[19] X. Song, T. Xu, L. Yang, Y. Li, Y. Yang, L. Jin, J. Zhang, R. Zhong, S. Sun, W. Zhao, Self-anticoagulant nanocomposite spheres for the removal of bilirubin from whole blood: a step toward a wearable artificial liver, Biomacromolecules 21 (5) (2020) 1762–1775, https://doi.org/10.1021/acs.biomac.9b01686.

[20] G. Baydemir, M. Andaç, N. Bereli, R. Say, A. Denizli, Selective removal of bilirubin from human plasma with bilirubin-imprinted particles, Ind. Eng. Chem. Res. 46 (9) (2007) 2843–2852, https://doi.org/10.1021/ie0611249.

[21] M. Syu, J. Deng, Y. Nian, T. Chiu, A. Wu, Binding specificity of α-bilirubin-imprinted poly(methacrylic acid-co-ethylene glycol dimethacrylate) toward α-bilirubin, Biomaterials 26 (22) (2005) 4684–4692, https://doi.org/10.1016/j.biomaterials.2004.11.024.

[22] A.S. Timin, A.V. Solomonov, I.I. Musabirov, S.N. Sergeev, S.P. Ivanov, E.V. Rumyantsev, Characterization and evaluation of silica particles coated by PVP and albumin for effective bilirubin removal, J. Sol. Gel Sci. Technol. 74 (1) (2015) 187–198, https://doi.org/10.1007/s10971-014-3595-y.

[23] X. Song, X. Huang, Z. Li, Z. Li, K. Wu, Y. Jiao, C. Zhou, Construction of blood compatible chitin/graphene oxide composite aerogel beads for the adsorption of bilirubin, Carbohydr. Polym. 207 (2019) 704–712, https://doi.org/10.1016/j.carbpol.2018.12.005.

[24] Q. Li, W. Zhao, H. Guo, J. Yang, J. Zhang, M. Liu, T. Xu, Y. Chen, L. Zhang, Metal-organic framework traps with record-high bilirubin removal capacity for hemoperfusion therapy, ACS Appl. Mater. Interfaces 12 (23) (2020) 25546–25556, https://doi.org/10.1021/acsami.0c03859.

[25] Y. Ma, J. Chen, J. Li, W. Han, Y. Chai, T. Wang, Q. Zhang, L. Wang, W. Wang, Z. Wang, Selective adsorption of bilirubin against albumin to alkylamine functionalized PVA microspheres, J. Biomater. Sci. Polym. Ed. 30 (5) (2019) 337–354, https://doi.org/10.1080/09205063.2018.1553104.

[26] V. Weber, I. Linsberger, M. Hauner, A. Leistner, A. Leistner, D. Falkenhagen, Neutral styrene divinylbenzene copolymers for adsorption of toxins in liver failure, Biomacromolecules 9 (4) (2008) 1322–1328, https://doi.org/10.1021/bm701396n.

[27] S. Harm, F. Gabor, J. Hartmann, Characterization of adsorbents for cytokine removal from blood in an in vitro model, J. Immunol. Resear. (2015), https://doi.org/10.1155/2015/484736.

[28] Y. Yu, Z. Mu, B. Jin, Z. Liu, R. Tang, Organic-inorganic copolymerization for a homogenous composite without an interphase boundary, Angew. Chem. Int. Ed. 59 (5) (2020) 2071–2075, https://doi.org/10.1002/anie.201913828.

[29] Y. Yang, Q. Zhang, T. Xu, H. Zhang, M. Zhang, L. Lu, Y. Hao, J.H. Fuh, X. Zhao, Photocrosslinkable nanocomposite ink for printing strong, biodegradable and bioactive bone graft, Biomaterials 263 (2020), https://doi.org/10.1016/j.biomaterials.2020.120378, 120378.

[30] H.A. Kim, B.K. Kim, Synthesis and properties of waterborne polyurethane/hydroxyapatite chemical hybrids, Prog. Org. Coating 128 (2019) 69–74, https://doi.org/10.1016/j.porgcoat.2018.12.009.

[31] C. Ye, Q. Gong, F. Lu, J. Liang, Preparation of carbon nanotubes/phenolic-resin-derived activated carbon spheres for the removal of middle molecular weight toxins, Separ. Purif. Technol. 61 (1) (2008) 9–14, https://doi.org/10.1016/j.seppur.2007.09.021.

[32] Y. Chai, J. Chen, T. Wang, J. Chen, Y. Ma, G. Cheng, C. Li, Q. Zhang, L. Ou, W. Li, Bead-type polystyrene/nano-CaCO₃ (PS/nCaCO₃) composite: a high-performance adsorbent for the removal of interleukin-6, J. Mater. Chem. B 7 (9) (2019) 1404–1414, https://doi.org/10.1039/C8TB02504E.

[33] X. Deng, J. Hao, C. Wang, Preparation and mechanical properties of nanocomposites of poly(d,l-lactide) with Ca-deficient hydroxyapatite nanocrystals, Biomaterials 22 (21) (2001) 2867–2873, https://doi.org/10.1016/S0142-9612(01)00031-X.

[34] K. Pielichowska, Polyoxymethylene-homopolymer/hydroxyapatite nanocomposites for biomedical applications, J. Appl. Polym. Sci. 123 (4) (2012) 2234–2243, https://doi.org/10.1002/app.34752.

[35] C. Stötzel, F.A. Müller, F. Reinert, F. Niederdraenk, J.E. Barralet, U. Gbureck, Ion adsorption behaviour of hydroxyapatite with different crystallinities, Colloids Surf. B Biointerfaces 74 (1) (2009) 91–95, https://doi.org/10.1016/j.colsurfb.2009.06.031.

[36] M. Boutinguiza, J. Pou, R. Comesaña, F. Lusquiños, A. de Carlos, B. León, Biological hydroxyapatite obtained from fish bones, Mater. Sci. Eng. C 32 (3) (2012) 478–486, https://doi.org/10.1016/j.msec.2011.11.021.

[37] J. Zhao, Y. Hao, L. Cao, J. Wang, W. Wang, X. Wu, Preparation of PHEMA/nHAP nanocomposites via in situ polymerization in supercritical carbon dioxide for biomedical applications, Fibers Polym. 18 (5) (2017) 868–874, https://doi.org/10.1007/s12221-017-1127-4.

[38] S. Harm, D. Falkenhagen, J. Hartmann, Pore size-a key property for selective toxin removal in blood purification, Int. J. Artif. Organs 37 (9) (2014) 668–678, https://doi.org/10.5301/ijao.5000354.

[39] A. Hosainzadeh, M. Gharanfoli, M.R. Saberi, J. Chamani, Probing the interaction of human serum albumin with bilirubin in the presence of aspirin by multi-

spectroscopic, molecular modeling and zeta potential techniques: insight on binary and ternary systems, J. Biomol. Struct. Dyn. 29 (5) (2012) 1013–1050, https://doi.org/10.1080/073911012010525029.

[40] L. Uzun, A. Denizli, Bilirubin removal performance of immobilized albumin in a magnetically stabilized fluidized bed, J. Biomater. Sci. Polym. Ed. 17 (7) (2006) 791–806, https://doi.org/10.1163/156856206777656481.

[41] M. Shi, C. Dong, Z. Wang, X. Tian, S. Zhao, J. Wang, Support surface pore structures matter: effects of support surface pore structures on the TFC gas separation membrane performance over a wide pressure range, Chin. J. Chem. Eng. 27 (8) (2019) 1807–1816, https://doi.org/10.1016/j.cjche.2018.12.009.

[42] T. Boyadzhieva, V. Koleva, R. Kukeva, D. Nihtianova, S. Harizanova, R. Stoyanova, Storage performance of Mg^{2+} substituted $NaMnPO_4$ with an olivine structure, RSC Adv. 10 (49) (2020) 29051–29060, https://doi.org/10.1039/D0RA05698G.

[43] M. Wang, T. Bao, W. Yan, D. Fang, Y. Yu, Z. Liu, G. Yin, M. Wan, C. Mao, D. Shi, Nanomotor-based adsorbent for blood Lead (II) removal in vitro and in pig models, Bioactive Mater. 6 (4) (2021) 1140–1149, https://doi.org/10.1016/j.bioactmat.2020.09.032.

[44] C. Zhao, W. Zhang, Preparation of waterborne polyurethane nanocomposites: polymerization from functionalized hydroxyapatite, Eur. Polym. J. 44 (7) (2008) 1988–1995, https://doi.org/10.1016/j.eurpolymj.2008.04.029.

[45] W. Shi, M. Xia, F. Wang, L. Dong, S. Zhu, Efficient absorption properties of surface grafted HEDP-HAP composites for Pb^{2+} and Cu^{2+}: experimental study and visualization study of interaction based on Becke surface analysis and independent gradient model, J. Hazard Mater. 401 (2021), https://doi.org/10.1016/j.jhazmat.2020.123748, 123748.

[46] W. Zhang, Y. Chai, N. Cao, Y. Wang, Synthesis and characterization of selenium substituted hydroxyapatite via a hydrothermal procedure, Mater. Lett. 134 (2014) 123–125, https://doi.org/10.1016/j.matlet.2014.07.072.

[47] N. Khurana, P. Arora, A.S. Pente, K.C. Pancholi, V. Kumar, C.P. Kaushik, S. Rattan, Surface modification of zinc oxide nanoparticles by vinyltriethoxy silane (VTES), Inorg. Chem. Commun. 124 (2021), https://doi.org/10.1016/j.inoche.2020.108347, 108347.

[48] S. Lan, L. Li, D. Xu, D. Zhu, Z. Liu, F. Nie, Surface modification of magnesium hydroxide using vinyltriethoxysilane by dry process, Appl. Surf. Sci. 382 (2016) 56–62, https://doi.org/10.1016/j.apsusc.2016.04.119.

[49] W. Wei, J. Cui, Z. Wei, Effects of low molecular weight organic acids on the immobilization of aqueous Pb (II) using phosphate rock and different crystallized hydroxyapatite, Chemosphere 105 (2014) 14–23, https://doi.org/10.1016/j.chemosphere.2013.09.121.

[50] W. Zhang, Y. Chai, X. Xu, Y. Wang, N. Cao, Rod-shaped hydroxyapatite with mesoporous structure as drug carriers for proteins, Appl. Surf. Sci. 322 (2014) 71–77, https://doi.org/10.1016/j.apsusc.2014.10.064.

[51] B. Yang, M. Li, Y. Wu, J. Huang, H. Zhang, C. Deng, Preparation and characterization of bone-like hydroxyapatite/poly (methyl methacrylate) composite biomaterials, Sci. Eng. Compos. Mater. 20 (2) (2013) 147–153, https://doi.org/10.1515/secm-2012-0079.

[52] A. Sionkowska, J. Kozłowska, Characterization of collagen/hydroxyapatite composite sponges as a potential bone substitute, Int. J. Biol. Macromol. 47 (4) (2010) 483–487, https://doi.org/10.1016/j.ijbiomac.2010.07.002.

[53] M.M. Hasan, M.N. Khan, P. Haque, M.M. Rahman, Novel alginate-di-aldehyde cross-linked gelatin/nano-hydroxyapatite bioscaffolds for soft tissue regeneration, Int. J. Biol. Macromol. 117 (2018) 1110–1117, https://doi.org/10.1016/j.ijbiomac.2018.06.020.

[54] Z. Feng, W. Wei, L. Wang, R. Hong, Cross-linked PS-DVB/Fe$_3$O$_4$ microspheres with quaternary ammonium groups and application in removal of nitrate from water, RSC Adv. 5 (117) (2015) 96911–96917, https://doi.org/10.1039/C5RA19642F.

[55] N. Pramanik, S. Mohapatra, P. Bhargava, P. Pramanik, Chemical synthesis and characterization of hydroxyapatite (HAp)-poly (ethylene co vinyl alcohol)(EVA) nanocomposite using a phosphonic acid coupling agent for orthopedic applications, Mater. Sci. Eng. C 29 (1) (2009) 228–236, https://doi.org/10.1016/j.msec.2008.06.013.

[56] Y. Fu, X. Huang, S. Zhong, W.J. Yi, L.J. Li, A new chloromethylation method based on polystyrene-divinylbenzene, Chem. Pap. 73 (9) (2019) 2183–2188, https://doi.org/10.1007/s11696-019-00761-6.

[57] M. Abbasian, A. Ghaderi, H. Namazi, A.A. Entezami, Preparation of anion-exchange resin based on styrene-divinylbenzene copolymer obtained by suspension polymerization method, Polymer-Pastics Technol. Eng. 50 (15) (2011) 1606–1612, https://doi.org/10.1080/03602559.2011.593088.

[58] S. Qin, L.Y. Ma, X. Sun, X. Mao, L. Xu, Hierarchically porous poly (ethylenimine) modified poly (styrene-co-divinylbenzene) microspheres for the adsorption of gold nanoparticles and simultaneously being transformed as the nanoparticles immobilized catalyst, J. Hazard Mater. 366 (2019) 529–537, https://doi.org/10.1016/j.jhazmat.2018.12.033.

[59] K. Murtada, F. de Andrés, Á. Ríos, M. Zougagh, A simple poly (styrene-co-divinylbenzene)-coated glass blood spot method for monitoring of seven antidepressants using capillary liquid chromatography-mass spectrometry, Talanta 188 (2018) 772–778, https://doi.org/10.1016/j.talanta.2018.06.059.

[60] Q. Li, S. Jin, B. Tan, Template-mediated synthesis of hollow mcroporous organic nanorods with tunable aspect ratio, Sci. Rep. 6 (1) (2016) 1–8, https://doi.org/10.1038/srep31359.

[61] N. Manikandan, XRD, FTIR and the optical studies of pure polystyrene film, Int. J. Recent Innov. Trends Comput. Commun. 2 (5) (2014) 1148–1151, https://doi.org/10.17762/ijritcc.v2i5.3128.

[62] M. Kassaee, E. Motamedi, M. Majdi, Magnetic Fe$_3$O$_4$-graphene oxide/polystyrene: fabrication and characterization of a promising nanocomposite, Chem. Eng. J. 172 (1) (2011) 540–549, https://doi.org/10.1016/j.cej.2011.05.093.

[63] M.R. Awual, New type mesoporous conjugate material for selective optical copper (II) ions monitoring & removal from polluted waters, Chem. Eng. J. 307 (2017) 85–94, https://doi.org/10.1016/j.cej.2016.07.110.

[64] Z. Li, Y. Cao, G. Li, L. Chen, W. Xu, M. Zhou, B. He, W. Wang, Z. Hou, High rate capability of S-doped ordered mesoporous carbon materials with directional arrangement of carbon layers and large d-spacing for sodium-ion battery, Electrochim. Acta 366 (2021), https://doi.org/10.1016/j.electacta.2020.137466, 137466.

[65] M. Salami, V.S. Gharahshiran, F. Fazlikhani, O. Mirzaee, Structural, morphological and magnetic properties investigation of magnetically separable mesoporous carbon, Mater. Chem. Phys. 257 (2021), https://doi.org/10.1016/j.matchemphys.2020.123694, 123694.

[66] P. Deb, E. Barua, S.D. Lala, A.B. Deoghare, Synthesis of hydroxyapatite from Labeo rohita fish scale for biomedical application, Mater. Today: Proc. 15 (2019) 277–283, https://doi.org/10.1016/j.matpr.2019.05.006.

[67] A. Farzadi, F. Bakhshi, M. Solati-Hashjin, M. Asadi-Eydivand, N.A. abu Osman, Magnesium incorporated hydroxyapatite: synthesis and structural properties characterization, Ceram. Int. 40 (4) (2014) 6021–6029, https://doi.org/10.1016/j.ceramint.2013.11.051.

[68] M.A. Goldberg, P.V. Protsenko, V.V. Smirnov, O.S. Antonova, S.V. Smirnov, A.A. Konovalov, K.G. Vorckachev, E.A. Kudryavtsev, S.M. Barinov, V.S. Komlev, The enhancement of hydroxyapatite thermal stability by Al doping, J. Mater. Resear. Technol. 9 (1) (2020) 76–88, https://doi.org/10.1016/j.jmrt.2019.10.032.

[69] X.J. Li, C.J. Yan, W.J. Luo, Q. Gao, Q. Zhou, C. Liu, S. Zhou, Exceptional cerium (III) adsorption performance of poly (acrylic acid) brushes-decorated attapulgite with abundant and highly accessible binding sites, Chem. Eng. J. 284 (2016) 333–342, https://doi.org/10.1016/j.cej.2015.09.003.

[70] L. Li, J. Zhao, Y. Sun, F. Yu, J. Ma, Ionically cross-linked sodium alginate/κ-carrageenan double-network gel beads with low-swelling, enhanced mechanical properties, and excellent adsorption performance, Chem. Eng. J. 372 (2019) 1091–1103, https://doi.org/10.1016/j.cej.2019.05.007.

[71] S. Inoue, K. Kiriyama, Y. Hatanaka, H. Kanoh, Adsorption properties of an activated carbon for 18 cytokines and HMGB1 from inflammatory model plasma, Colloids Surf. B Biointerfaces 126 (2015) 58–62, https://doi.org/10.1016/j.colsurfb.2014.12.015.

[72] Q. Gao, B. Han, Three-dimensionally porous graphene: a high-performance adsorbent for removal of albumin-bonded bilirubin, Colloids Surf. B Biointerfaces 149 (2017) 146–153, https://doi.org/10.1016/j.colsurfb.2016.10.015.

[73] K. Yamazaki, K. Shinke, T. Ogino, Selective adsorption of bilirubin against albumin to oxidized single-wall carbon nanohorns, Colloids Surf. B Biointerfaces 112 (2013) 103–107, https://doi.org/10.1016/j.colsurfb.2013.07.064.

[74] J. Ostrow, P. Mukerjee, C. Tiribelli, Structure and binding of unconjugated bilirubin: relevance for physiological and pathophysiological function, JLR (J. Lipid Res.) 35 (10) (1994) 1715–1737, https://doi.org/10.1016/S0022-2275(20)39768-6.

[75] C. Zhou, Q. Gao, S. Wang, Y. Gong, K. Xia, B. Han, M. Li, Y. Ling, Remarkable performance of magnetized chitosan-decorated lignocellulose fiber towards biosorptive removal of acidic azo colorant from aqueous environment, React. Funct. Polym. 100 (2016) 97–106, https://doi.org/10.1016/j.reactfunctpolym.2015.11.010.

[76] C. Chen, D. Chen, S. Xie, H. Quan, X. Luo, L. Guo, Adsorption behaviors of organic micropollutants on zirconium metal-organic framework UiO-66: analysis of surface interactions, ACS Appl. Mater. Interfaces 9 (46) (2017) 41043–41054, https://doi.org/10.1021/acsami.7b13443.

[77] V. Nikolaev, V. Sarnatskaya, V. Sigal, V. Klevtsov, K. Makhorin, L. Yushko, High-porosity activated carbons for bilirubin removal, Int. J. Artif. Organs 14 (3) (1991) 179–185, https://doi.org/10.1177/039139889101400311.

[78] P. Veverka, K. Jeřábek, Mechanism of hypercrosslinking of chloromethylated styrene-divinylbenzene copolymers, React. Funct. Polym. 41 (1–3) (1999) 21–25, https://doi.org/10.1016/S1381-5148(99)00030-9.

[79] J. Jacobsen, R. Brodersen, Albumin-bilirubin binding mechanism, J. Biol. Chem. 258 (10) (1983) 6319–6326, https://doi.org/10.1016/S0021-9258(18)32411-6.

[80] A. Asfaram, M. Fathi, S. Khodadoust, M. Naraki, Removal of direct Red 12B by garlic peel as a cheap adsorbent: kinetics, thermodynamic and equilibrium isotherms study of removal, Spectrochim. Acta Mol. Biomol. Spectrosc. 127 (2014) 415–421, https://doi.org/10.1016/j.saa.2014.02.092.

[81] S. Huang, J. Zheng, Y. Zhang, J. Zheng, Z. Zhuang, Q. Yang, F. Wang, G. Chen, S. Huang, G. Ouyang, Polydopamine decorated ordered mesoporous carbon for efficient removal of bilirubin under albumin-rich conditions, J. Mater. Chem. B 8 (2) (2020) 290–297, https://doi.org/10.1039/C9TB02147G.

[82] G.K. Michalopoulos, L. Barua, W.C. Bowen, Transdifferentiation of rat hepatocytes into biliary cells after bile duct ligation and toxic biliary injury, Hepatology 41 (3) (2005) 535–544, https://doi.org/10.1002/hep.20600.

[83] J.L. Xia, C. Dai, G.K. Michalopoulos, Y. Liu, Hepatocyte growth factor attenuates liver fibrosis induced by bile duct ligation, Am. J. Pathol. 168 (5) (2006) 1500–1512, https://doi.org/10.2353/ajpath.2006.050747.

[84] Y. Xiang, Z. Bai, S. Zhang, Y. Sun, S. Wang, X. Wei, W. Mo, J. Long, Z. Liu, C. Yang, Lead adsorption, anticoagulation and in vivo toxicity studies on the new magnetic nanomaterial Fe$_3$O$_4$@SiO$_2$@DMSA as a hemoperfusion adsorbent, Nanomed. Nanotechnol. Biol. Med. 13 (4) (2017) 1341–1351, https://doi.org/10.1016/j.nano.2017.01.007.